Comprehensive study on the effect of magnesium loading over Nickel-ordered mesoporous alumina for dry reforming of methane

Leila Karam, Marco Armandi, Sandra Casale, Vanessa El Khoury, Barbara Bonelli, Pascale Massiani, Nissrine El Hassan

Comprehensive study on the effect of magnesium loading over Nickel-ordered mesoporous alumina for dry reforming of methane

Leila Karam[a,b], Marco Armandi[c], Sandra Casale[a], Vanessa El Khoury[b], Barbara Bonelli[c], Pascale Massiani[a] and Nissrine El Hassan[b]***

[a] Sorbonne Université, Campus Pierre et Marie Curie, Laboratoire de Réactivité de Surface, UMR CNRS 7197, 4 Place Jussieu, F-75005 Paris, France

[b] Department of Chemical Engineering, Faculty of Engineering, University of Balamand, P.O. Box 33, Amioun, 33 El Koura, Lebanon

[c] Dipartimento di Scienza dei Materiali ed Ingegneria Chimica and INSTM Unit of Torino-Politecnico, Politecnico di Torino, C.so Duca degli Abruzzi 24, I-10129 Torino, Italy

Corresponding authors

[*]pascale.massiani@upmc.fr

[**]nissrine.hassan@balamand.edu.lb

Abstract

A comprehensive study of the effect of Mg loading on the performances in Dry Reforming of Methane of a series of mesoporous Ni_6-Mg_x-Al_2O_3 catalysts containing 6 wt% Ni and 0 to 26 wt% Mg is presented. Complementary characterizations by N_2 sorption, XRD, SEM/TEM, FT-IR, H_2-TPR and H_2-TPD of the materials, synthesized by one-pot EISA method and studied in their calcined and reduced forms, reveal excellent porous ordering and high and homogeneous chemicals distribution up to an intermediate Mg content, afterwards MgO segregation occurs,

associated to some structural loss, nickel sintering due to the disappearance of the stabilizing nickel aluminate species, and to strong basic sites formation. In line with these physicochemical changes, all catalytic results reveal the existence of volcano curves in which the optimum Mg content is between 5 and 10 wt%. This optimum is also discussed in view of turn over frequencies and activation energy values.

Keywords: nickel, magnesium, mesoporous alumina, basicity, dry reforming of methane, carbon dioxide

1. Introduction

Dry reforming of methane (DRM) is a reaction that converts CH_4 and CO_2 into syngas, a mixture of H_2 and CO. Compared to steam reforming of methane (SRM), it offers the advantage to use CO_2 as reactant instead of steam, allowing the valorization of this greenhouse gas, which is more environmental friendly than CO_2 storage underground [1]. Moreover, the H_2:CO molar ratio produced in the obtained syngas (1 with DRM instead of 3 with SRM) is better suited for a direct utilization in Fischer-Tropsch synthesis. Nowadays, best catalysts for DRM are still based on noble metals (Pt, Ir, Pd, Ru and Rh) [2, 3] and there is a need to move to cheaper and more available active phases, especially transition metals. Amongst them, nickel is the most promising one and shows high activity, but the development of efficient and economical DRM Ni-based catalysts applicable to industry remains a challenge because they suffer from rapid deactivation by nickel sintering and carbon deposition [3, 4].

In order to improve the stability of nickel catalysts in DRM, different strategies have been developed including changing the type of support [5-8], altering the size of the nickel particles [6, 9], employing a second active phase (usually small amount of noble metal) [10, 11] or modifying the synthesis mode [8, 12-14]. Mesoporous supports like silica (SBA-15) [13, 15] and alumina (Al_2O_3) [16] have been shown to play a crucial role in stabilizing the nickel nanoparticles inside the porosity by confinement effects. The benefits of nickel confinement were similarly recently highlighted in the case of boron nitride interface-confined and LDHs-derived Ni catalysts in which defects were also shown to play a role [17]. Moreover, creating Lewis basic centers in the material by adding an alkali, alkaline earth or rare earth metal oxide [18-21] was found to enhance the catalytic stability by minimizing carbon formation. Indeed, these sites favor the adsorptive decomposition of CO_2 on the catalyst surface and promote the

oxidation of the carbon deposits [9]. Amongst such additives, MgO has the advantages of availability and well-known basic properties. Moreover, it has a similar crystal structure than that of NiO, which can lead to a NiO-MgO solid solution able to strengthen the interaction with the support and in turn increase nickel nanoparticles stability [22].

Table 1 gathers a set of bibliographic data on nickel-magnesium supported on mesoporous alumina catalysts applied in DRM. The catalysts differ by their metal compositions and by their preparation routes. The simplest and most conventional one is wetness impregnation that is widely applied but leads to unsatisfying metal anchorage and stability in the harsh conditions of DRM [20, 21]. More elaborated strategies include sol-gel [22], two-step hydrothermal [23] or co-precipitation [24, 25]. Even if efficient for obtaining active DRM catalysts, most of these methods suffer from certain technical deficiencies like the need of a long preparation time [21, 23, 25], tough conditions [22, 23], hard or multi operation steps [23, 25] or expensive substrates [23]. Basic hydrotalcites containing both nickel and magnesium were also prepared by co-precipitation and tested in DRM, but the catalysts were not stable because of a lack of porosity and of a weak metal-support interaction resulting in fast nickel sintering and carbon deposition [27]. Compared to these strategies, the one-pot (one-step) evaporation induced self-assembly (EISA) method has the advantages to be rapid, easy and low cost [28]. It consists in adding magnesium and nickel directly in the synthesis medium of the alumina and led to mesoporous nickel-magnesium-alumina catalysts with high nickel dispersion and excellent stability in DRM (Table 1) [29]. This technique was also developed to mix all metals in the synthesis medium of mesoporous alumina such as Ni alone [30], Ni and Ce [31], and Ni and Co [32].

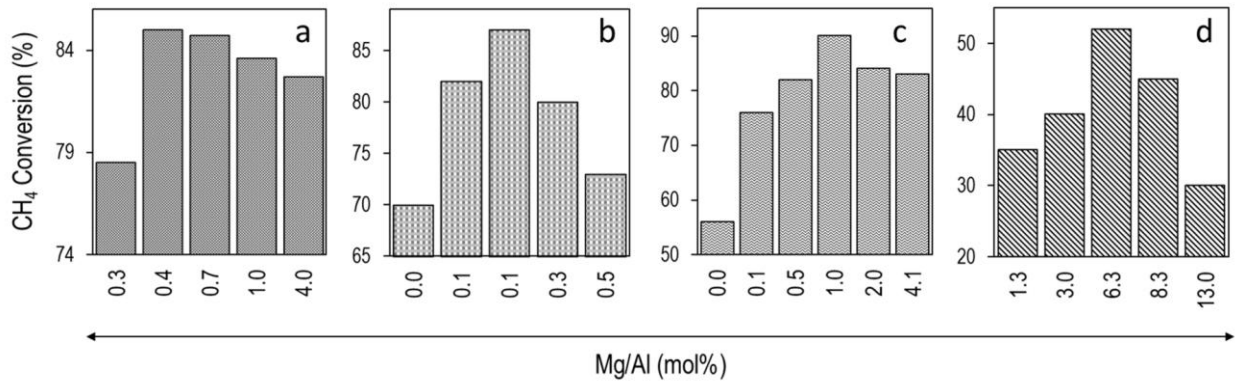

Figure 1: Evolution of CH_4 conversion in DRM as a function of Mg content in series of Ni-Mg_x-Al_2O_3 catalysts described in the literature and prepared by (a,b) co-precipitation [24, 25], (c) sol-gel [22] and (d) two-step hydrothermal [23] routes.

Considering this state-of-the-art on nickel-magnesium-alumina DRM catalysts, and regardless of the preparation protocol used, the highest activity systematically appears at intermediate magnesium content. This is illustrated by the histograms shown in Figure 1 that report, for a selection of representative literature data, the evolution of the CH_4 conversion as a function of the Mg/Al atomic ratio. Even if the optimal Mg content varies depending on the preparation method, and hence on the distinct textural and structural properties obtained, it is clear that Mg addition is favorable up to a certain content, afterwards the activity progressively decreases. Although the existence of such behavior was already noted by few authors, it was to our knowledge never comprehensively analyzed and neither discussed in view of the evolution of the physicochemical properties upon magnesium addition.

Table 1

In this context, the purpose of this work was to elaborate a systematic study aiming to understand the reasons for such occurrence of an optimized Mg content. To this end, we prepared a series of mesoporous Ni_6-Mg_x-Al_2O_3 materials containing a constant nickel loading around 6 wt% (chosen from our previous works [13, 15, 33]) but an increasing amount of basic Mg modifier that was varied over a wide percentage range (0, 5, 7, 15 and 26 wt%). We selected the EISA-one-pot synthesis as preparation route in order to benefit of the simplicity of the method and of its proven efficiency for producing highly active methane reforming catalysts [33]. The prepared samples were characterized in their fresh and reduced states. They were tested at 650 °C in DRM using a conventional model reactants mixture made of methane and carbon dioxide in an equimolar ratio. Attention was paid to carry out the catalytic tests under conditions providing conversions far from thermodynamic equilibrium to allow reliable comparison of performances between the catalysts.

2. Experimental

2.1 Materials

Mesoporous Ni_6-Mg_x-Al_2O_3 samples with c.a. 6 wt% of Ni and x wt% of Mg (x = 0, 5, 7, 15 or 26) were synthesized using the developed one-pot evaporation induced self-assembly (EISA) method established elsewhere [33-35]. All chemicals were used as received without additional purification. A typical synthesis involved dissolving 1 g of P123 Pluronic triblock copolymer ($EO_{20}PO_{70}EO_{20}$, M_n=5800, Sigma-Aldrich, 435465) in 20 mL of absolute ethanol (CH_3CH_2OH, M_n=46.07, Sigma-Aldrich, 64175) at ambient temperature (25 °C) under intense stirring. 1.6 mL of 65 wt% nitric acid (HNO_3, M_n=63.01, Johnson Matthey S.A) was then added to the solution,

still under stirring, simultaneously with A mmol of aluminum isopropoxide ($Al[OCH(CH_3)_2]_3$, M_n=204.24, Sigma-Aldrich, 220418), B mmol of nickel nitrate hexahydrate ($Ni(NO_3)_2.6H_2O$, Mn=290.79, Sigma-Aldrich, 72253), and C mmol of magnesium nitrate hexahydrate ($Mg(NO_3)_2 \cdot 6H_2O$, M_n=256.41, Sigma-Aldrich, 203696). For each preparation, the values of A, B and C were established as to keep the total molar composition (Ni + Mg + Al) constant and equal to 10 mmol. The obtained mixture was covered with a polyethylene film (PE) and kept under stirring overnight to reach a complete dissolution of the chemicals added. Next, the solution was dried at 60 °C for 48 h to slowly evaporate ethanol and HNO_3 with the aid of a Julabo connected to two plastic tubes that circulates water to regulate and control the temperature. The resulting Xerogels were calcined in a muffle furnace under air at 600 °C for 5 h with a heating rate of 0.5 $°C.min^{-1}$ (thin bed conditions), giving the series of Ni_6-Mg_x-Al_2O_3 materials. For the sake of comparison, two Ni free reference samples (Al_2O_3 and Mg_{26}-Al_2O_3) were also synthesized using the same procedure except for the addition of Ni.

2.2 Characterizations

N_2 adsorption-desorption isotherms were recorded at -196 °C using an ASAP 2020 Micromeritics apparatus. The samples were first degassed under vacuum for 2 h at 250 °C in a cell before inserting it in liquid nitrogen. After plotting the N_2-isotherm, the specific area (SA) of each catalyst was calculated from BET (Brunauer-Emmet-Teller) equation at a relative pressure between 0.05 and 0.25. The corresponding single point total pore volume (PV) was obtained from the sorption branch at a relative pressure of 0.99. The pore size distribution and mean pore size (Φ_{pore}) were calculated based on the BJH (Barrett-Joyner-Halenda) formula which was applied on the desorption branch.

Powder X-rays diffraction (XRD) patterns were registered at small and wide angles to determine the structural properties of both the supports and nickel metal phases. Small angles data were obtained on a BRUKER type D8 ADVANCE diffractometer equipped with a CuKα irradiation source (λ equal to 1.5405 nm) and operating at 40 kV and 30 mA, with a 2θ range of 0.5° to 4° and a time step of 1 s. For each calcined sample, the unit cell parameter a_0 was calculated from the equation $a_0= 2d_{100}/\sqrt{3}$ where d_{100} is the inter-reticular distance of plan [100] derived from the main peak position ($d= \lambda/2\sin\theta$) and t (nm) is the pore wall thickness ($t=a_0-D_{BJH}$, where D_{BJH} is the pore diameter obtained from N_2 sorption isotherms). Wide angles diffractograms were obtained on a PANalytical XPert^3 instrument still using a CuKα radiation and operating at a voltage of 30 Kv, a current of 10 mA, a 2θ range 20° to 90° and a time step of 2 s. Crystalline phases were identified from standard ICDD (international center for diffraction data) powder XRD files. After phases identification, mean crystallite sizes (Φ) of nickel-based nanoparticles were calculated using the Scherer's equation $D_{hkl}=K\lambda/\beta\cos\theta$, where K is the shape factor of the average spherical crystals, λ is the wavelength (1.5405 nm for CuKα), β is the full width at half maximum (FWHM) and θ is the peak position.

XPS spectra were obtained on an Omicron (ESCA+) X-ray photoelectron spectrometer with an Al Kα (hν =1486.6 eV) X-ray source having a 300 W electron beam power. The sample was evacuated under a vacuum of less than 10^{-10} mbar, then a monochromatic X-ray (Al Kα) irradiated the sample and excited the electrons. Surface compositions were determined by attributing the observed energy peaks to a specific element and quantifying their area using the Casa XPS software.

For infra-red measurements, the powders were pressed as thin self-supporting wafers and treated under secondary vacuum at 773 K for 3 h within a homemade quartz cell equipped with IR

transparent KBr windows. The FT-IR spectra were recorded after CO_2 adsorption (ca. 7.5 kPa equilibrium pressure) followed by evacuation at room temperature (r.t.), then at 100 °C and finally at 200 °C (duration of 1 h at each evacuation step). They were registered at a 2 cm^{-1} resolution on a BRUKER EQUINOX-55 spectrometer equipped with a mercury cadmium telluride (MCT) cryodetector. They were normalized with respect to the wafers optical density (ca. 10 mg cm^{-2}). The spectra are reported as difference spectra obtained by subtracting the IR spectrum of the naked sample (*i.e.* before CO_2 adsorption).

Hydrogen temperature programmed reduction (H_2-TPR) measurements were operated using an Autochem 2920 Micromeritics unit. A certain amount (70 mg) of calcined sample was put in a U-shaped quartz reactor and heated at a constant rate of 10 °C.min^{-1} from ambient temperature (25 °C) up to 900 °C. Reduction was performed under a 5 vol% H_2/Ar flow (25 mL.min^{-1}) and the amount of hydrogen consumed was constantly followed through a thermal conductivity detector (TCD). Before reaching this stage, the effluent gas was passed in a tube placed in a cold bath composed of ice and NaCl to trap any possible water formed during reaction ($H_{2(g)}+NiO_{(s)}\rightarrow Ni^0_{(s)}+H_2O_{(g)}$) and assert on the sole detection of H_2 consumption. This consumption was also used to evaluate the Ni contents in the materials, assuming a consumption of one H_2 per nickel (supposed to be at its Ni^{2+} oxidation state). Ni contents were also measured by X-Ray Fluorescence (XRF) analysis on an XEPOS spectrometer (Spectro Ametek) using a MicroPowder method and a calibration curve previously established from NiO and alumina mixtures of known compositions.

Hydrogen temperature programmed desorption (H_2-TPD) was applied using also the Autochem 2920 instrument, Micromeritics. The calcined sample (250 mg) was charged in a U-tube quartz reactor and reduced *in situ* at conditions similar to those applied before catalytic test (650 °C under

30 mL.min^{-1} 10%H_2/90%Ar for 2 h). The reactor was then cooled to 40 °C (still under the same reducing flow) and held at that temperature for 30 min in 30 mL.min^{-1} pure Ar to cast weakly bound hydrogen. The temperature was then increased again until 900 °C at a rate of 10 °C.min^{-1} under flowing Ar (30 mL.min^{-1}) while simultaneously measuring the amount of H_2 desorbed by TCD. The number of surface metal sites deduced from the area under the TPD curves was calculated by considering spherical nanoparticles and a stoichiometry of 1 H atom per 1 surface metal site.

Scanning electron microscopy (SEM) pictures were registered on the Hitachi SU-70 SEM-FEG microscope with an electron acceleration tension of 7 kV. Images were recorded in a mixed in-lens mode detector (70% secondary electrons and 30% backscattered electrons) to obtain simultaneous information about the surface morphology of the grains and the chemical contrast of nickel particles. High-resolution transmission electron microscopy (HR-TEM) experiments were performed on a JEOL-JEM 2100Plus electron microscope operating at 200 keV (LaB_6 gun). Preparation of the samples were done with a Leica ultra-microtome (50-60 nm thickness) on copper grids coated with a carbon membrane in order to visualize the dispersion of nickel nanoparticles within the mesoporous Ni_6-Mg_x-Al_2O_3 materials and to depict eventual carbon deposition inside or outside the pores. The “Comptage de Particules” software available at LRS was used to estimate the average size of nickel (Ni^0) nanoparticles. Around 500 particles were measured for a good size statistic. Mapping of the Al, Ni and Mg elements in the mesoporous supports were collected by combining HAADF-STEM (high angular annular dark field scanning transmission electron microscopy) and EDX spectra (SDD 80mm^2,Oxford Aztec software).

2.3 Catalytic tests

All prepared catalysts were tested in a Microactivity (MAR, PID Eng and Tech Spain) vertical fixed-bed Hastelloy-X tubular reactor having an internal diameter of 9 mm. Prior to catalytic test, each powder was loaded into the reactor and treated *in-situ* at 650 °C for 2 h under a 5 vol% H_2/Ar flow (volumetric flow rate of 30 mL.min^{-1}) to reduce nickel oxide into Ni^0 that is the nickel active state for DRM. The temperature was next cooled down to 250 °C, then the equimolar CH_4 and CO_2 reactant mixture was fed continuously into the reactor at atmospheric pressure (1 atm.) and under a hourly-space-velocities (GHSV) equal to either 36 or 180 L.g^{-1}.h^{-1} (using 100 mg and 20 mg of catalysts, respectively). Activity measurements were done while raising again the temperature from 200 °C to 750 °C at a constant temperature rate of 5 °C.min^{-1}, then the temperature was decreased at 650°C to perform stability tests for either 12 or 48 h. Some experiments were also done in the temperature range of 550-700°C (GHSV of 540 L.g^{-1}.h^{-1}) to estimate activation energies (E_a) from Arrhenius plots by increasing the temperature and measuring the conversion at each step after 60 min time on stream to ensure stable performance. Before analyzing the products, the effluent gas mixture was sent to a gas-liquid separator in order to condense any steam that might be formed during reaction. An online micro gas chromatography (Inficon) was used to analyze the outlet gaseous mixture composition. This Micro-GC contained a thermal conductivity detector (TCD) and two parallel columns (Plot U column and Molecular Sieve column) for the detection of CH_4, CO_2, H_2, and CO. The conversions of CH_4 (X_{CH4}) and CO_2 (X_{CO2}) as well as the H_2/CO molar ratio were calculated according to the formulas (eq. 1-3):

$$X_{CH4}\ (\%)=\frac{CH_{4(in)}-CH_{4(out)}}{CH_{4(in)}}\times 100 \qquad (1)$$

$$X_{CO2}\ (\%)=\frac{CO_{2(in)}-CO_{2(out)}}{CO_{2(in)}}\times 100 \qquad (2)$$

$$\frac{H_2}{CO}\ \text{molar ratio} = \frac{\text{mol of } H_2}{\text{mol of CO}} \quad (3)$$

The turnover frequencies (TOF), defined as the number of CH_4 (resp. CO_2) molecules converted over each surface metal site per second were also calculated (eq. 4) as:

$$\text{TOF}\ (s^{-1}) = \frac{Fi}{m_c} \times \frac{Xi}{100} \times \frac{1}{M_s} \quad (4)$$

where Fi is the Flow rate ($mol.s^{-1}$) of CH_4 (resp. CO_2), m_c is the catalyst weight (g), Xi is the conversion of CH_4 (resp. CO_2) and M_s is the number of surface metal site of the catalyst ($mol.g^{-1}$) obtained from H_2-TPD. Thermodynamic equilibrium curves were evaluated using the HSC 7.1 software and considering the presence of reactants and main products (CH_4, CO_2, H2, and CO) with argon (Ar) added as diluent.

3. Results

3.1 N_2 physisorption

All prepared materials exhibit a type IV nitrogen adsorption/desorption isotherm with H1 hysteresis loop (Fig. 2) characteristic of mesoporous materials [36]. The calcined samples having a magnesium weight percent between 0 and 7 wt% (Fig. 2Aa-d) show a very steep hysteresis loop typical of the presence of uniform cylindrically shaped mesopores [35, 36]. Higher Mg contents (samples Ni_6-Mg_{15}-Al_2O_3 and Ni_6-Mg_{26}-Al_2O_3, Fig. 2Ae,f) induce a decrease in the steepness of the loop and a shift to higher relative pressure, characteristic of more disordered and larger mesopores [35, 37]. This is also illustrated by the pore sizes ranges (inset in Fig. 2A) and mean pore sizes (Table 2) estimated after deriving BJH curves from the desorption part of the N_2-sorption isotherms. Thus, pore size distributions are narrow and with a mean size below 5.8

nm in the calcined samples with limited Mg content (≤ 7 wt%), but broader and shifted towards higher pores diameters (reaching a mean pore diameter of 7.4 nm) for both Mg-richest samples. Concomitantly, the specific surfaces are lower in the Mg-rich materials, by about 20% compared to the mesoporous reference alumina support (Table 2). Despite these differences, the total pore volumes are close in all calcined solids, between 0.47 and 0.52 $cm^3.g^{-1}$ (Table 2).

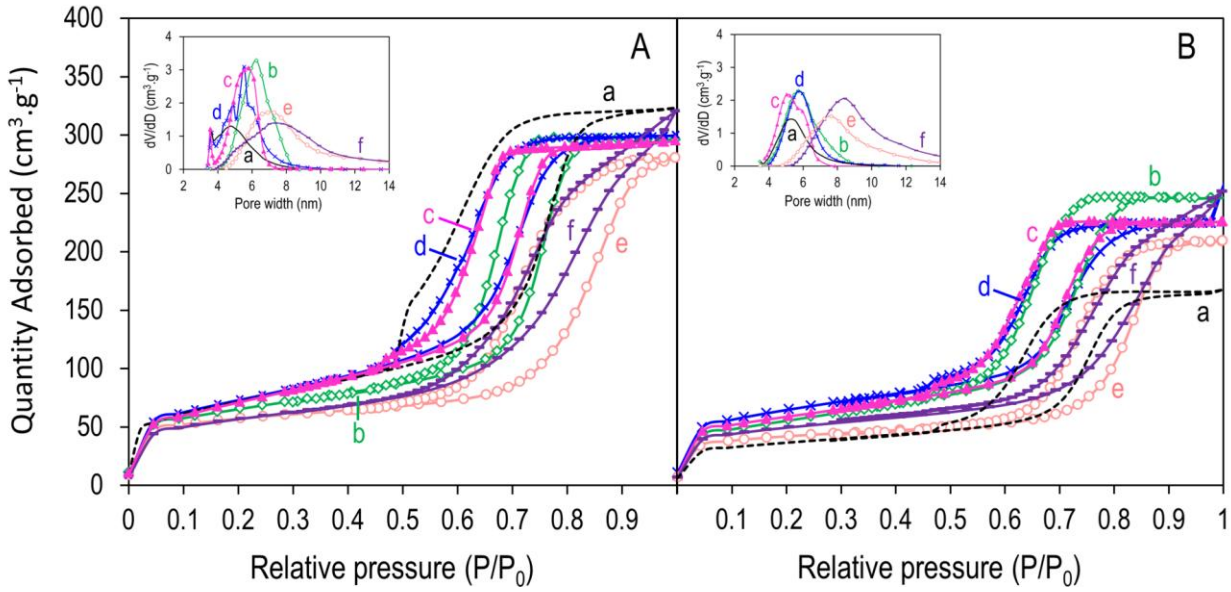

Figure 2: N_2 adsorption-desorption isotherms of (A) calcined and (B) reduced samples (a) Al_2O_3, (b) Ni_6-Al_2O_3, (c) Ni_6-Mg_5-Al_2O_3, (d) Ni_6-Mg_7-Al_2O_3, (e) Ni_6-Mg_{15}-Al_2O_3, (f) Ni_6-Mg_{26}-Al_2O_3

Table 2

Looking into more details, it can also be seen that the physisorption curve for the pure Al_2O_3 sample (Fig. 2Aa) shows a second small desorption step at low relative partial pressure (P/P_0=0.5), which is characteristic of the occurrence of restrictions creating ink-bottle sections within the channels [38, 39]. This reveals a lower structural quality for this Ni-free and Mg-free material, also confirmed by its lower stability upon reduction, as shown by the decrease of about

half of its surface area and pores volume after high temperature reduction treatment (Fig. 2Ba and Table 2). By comparison, the decrease is much less important for all other reduced samples whose shapes of isotherms moreover keep unchanged (Fig. 2B). The porous characteristics are thus globally preserved in the reduced catalysts except for a small shrinkage of the skeleton leading to slightly lower specific area and pore volume (Table 2).

3.2 Small and Wide angles X-rays diffraction

The structure ordering in the prepared samples was verified by small angle X-rays diffraction. For all calcined samples having a Mg content from 0 to 7 wt% (Fig. 3Aa-d), a diffraction peak at 2θ around 0.7-0.9° is systematically seen, together with a weaker peak at around 1.5-1.7°, typical respectively of the [100] and [110] plane reflections of hexagonally ordered mesopores with *p6mm* symmetry [35]. These peaks are more intense for calcined Ni_6-Mg_5-Al_2O_3 and Ni_6-Mg_7-Al_2O_3 (Fig. 3Ac,d) - and to a lower extent for calcined Ni_6-Al_2O_3 (Fig. 3Ab) - than for calcined Al_2O_3 (Fig. 3Aa). This reveals a more uniform hexagonal arrangement in presence of nickel and/or magnesium, also associated to slightly smaller unit cells and thinner walls (Table 2) as deduced from the slight shifts of the peaks towards higher angles. These trends agree with previous literature reporting that Mg^{2+} ions trigger certain interaction between the non-ionic surfactant P123 and metal ions (here Ni^{2+} and Mg^{2+}), leading to better ordered structures [37, 40]. After reduction, this hexagonal ordering in Ni_6-Al_2O_3, Ni_6-Mg_5-Al_2O_3 and Ni_6-Mg_7-Al_2O_3 is preserved, as shown by the persistence of diffraction bands, even if their weak intensity and broadening, till disappearance for the weaker one, indicate some loss of structural organization (Fig. 3A'a-d). Conversely, no diffraction peaks at small angles, and hence no pores ordering, are detected for both Mg-richer Ni_6-Mg_{15}-Al_2O_3 and Ni_6-Mg_{26}-Al_2O_3 materials, neither in their calcined (Fig. 3Ae,f) nor in their reduced states (Fig. 3A'e,f).

X-rays diffraction patterns were also registered at wide angles to get information on the small crystalline domains existing in the all Ni_6-Mg_x-Al_2O_3 series of materials. For the calcined samples with 7 wt% Mg or less (Fig. 3Ba-d), only a very broad and weak signal of amorphous alumina is visible (between 20° and 35°) and no peaks of crystalline NiO or MgO are detected, indicating that all species constituting the material are either highly dispersed or amorphous. Adding higher Mg amounts contributes to the appearance of diffraction peaks at 2θ equal to 37°, 43°, 63°, 75°, and 78° assignable to the (111), (200), (220), (311) and (222) reticular plans of crystalline MgO, respectively (JCPDS: 78-0430). The peaks are very weak and broad for Ni_6-Mg_{15}-Al_2O_3 (Fig. 3Be), revealing very small crystalline domains, but they are intense and thinner for Ni_6-Mg_{26}-Al_2O_3 (Fig. 3Bf) indicating the presence of MgO crystallites of about 5 nm is size. Still, no peaks attributable to Ni-based crystallites are detected.

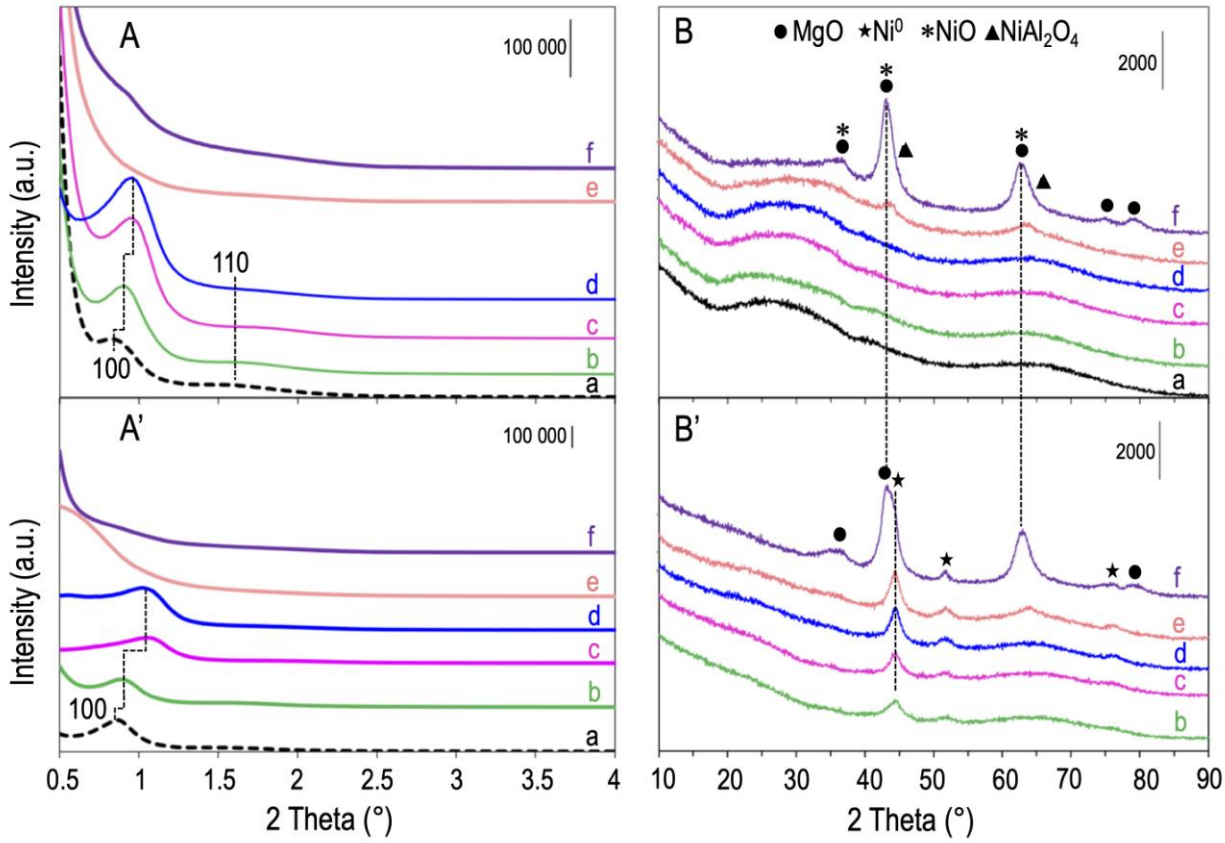

Figure 3: (A,A') Low and (B,B') wide angles XRD patterns of ((A-B) calcined and (A'-B') reduced samples (a) Al_2O_3, (b) Ni_6-Al_2O_3, (c) Ni_6-Mg_5-Al_2O_3, (d) Ni_6-Mg_7-Al_2O_3, (e) Ni_6-Mg_{15}-Al_2O_3 and (f) Ni_6-Mg_{26}-Al_2O_3.

Contrarily, nickel nanoparticles become visible in all materials after reduction (except in Ni-free Al_2O_3 and Mg_{26}-Al_2O_3) in the form of XRD peaks located at 44°, 52° and 76° (indexed with a star, Fig. 3B') typical of metallic Ni^0 with face centered cubic (FCC) unit cell (JCPDS: 03-065-0380). These peaks are the only ones distinctly detected in the patterns of the reduced catalysts (Fig. 3a-e) except for reduced Ni_6-Mg_{26}-Al_2O_3 (Fig. 3f) for which most of the peaks are superimposed to those of MgO, except for the signal at 52°. The latter was chosen for calculating the mean Ni^0 particles sizes by Scherer's equation. The obtained values are small in most catalysts, between 4 and 5 nm, and bigger in reduced Ni_6-Mg_{26}-Al_2O_3 where the mean size reaches 7.7 nm (Table 2).

3.3 XPS spectroscopy

Further insights on the characteristics of the Ni and Mg species were obtained by XPS and FT-IR spectroscopies applied to a selection of calcined materials.

Figure 4 shows the XPS spectra of Ni_6-Al_2O_3, Ni_6-Mg_7-Al_2O_3 and Ni_6- Mg_{26}-Al_2O_3. In the 850-890 eV region, they all exhibit the same series of four bands, characteristic of $Ni2p_{3/2}$ transitions (Fig. 4A). Their intensities are similar, whatever the sample is. They correspond to an atomic Ni content of c.a. 2 %, below the expected 5 % atomic content in the materials (Table 2). This suggests the absence of nickel segregation on the surface of the alumina grains. Peaks positions are also identical, with a main $Ni2p_{3/2}$ signature at around 856 eV (with its satellite at 863 eV). Such binding energy is significantly higher than that expected in free NiO (around 853 eV) [41] and is rather assignable to a $NiAl_2O_4$ spinel phase in which nickel is in strong interaction with a locally

structured Ni and Al environment [42]. In the 1300-1320 eV range, a band centered at 1304 eV typical of divalent magnesium (Mg^{2+}) in an oxygen-rich environment (here the mixed Mg-Al-oxide lattice) is also visible for Ni_6-Mg_7-Al_2O_3 (Fig. 4Bb). It is about 3.5 times more intense for Ni_6- Mg_{26}-Al_2O_3, in agreement with its higher Mg loading (Fig. 4Bc), and on the contrary absent for Ni_6-Al_2O_3, as expected from the absence of Mg in this sample (Fig. 4Ba).

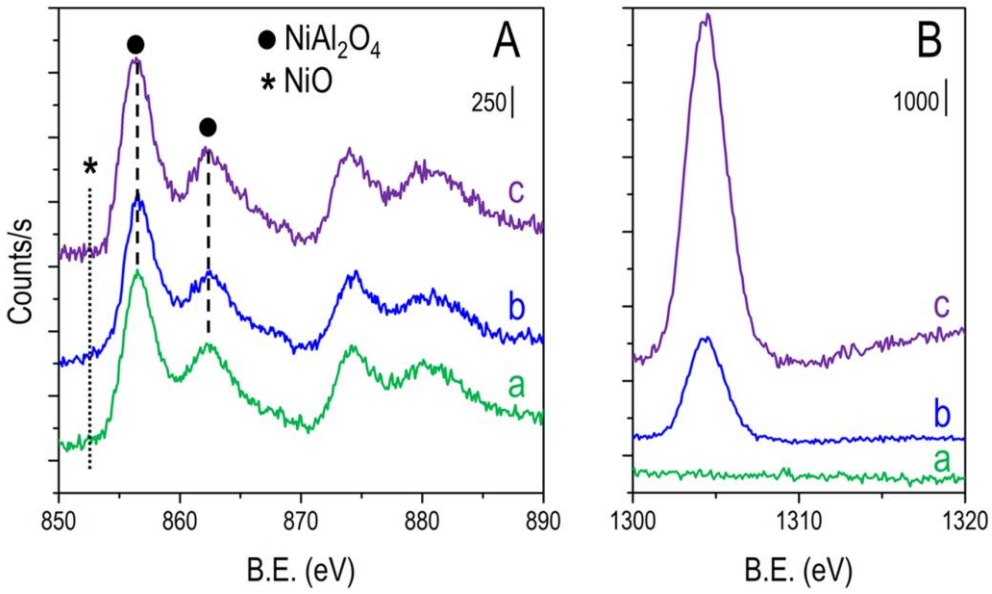

Figure 4: XPS spectra in the ranges (A) 850-890 eV (Ni element) and (B) 1300-1320 eV (Mg element) of calcined samples (a) Ni_6-Al_2O_3, (b) Ni_6-Mg_7-Al_2O_3 and (c) Ni_6-Mg_{26}-Al_2O_3.

3.4 FT-IR spectroscopy

CO_2 is often used as a probe molecule able to form carbonates upon interaction with basic sites. Its propensity to be adsorbed on the series of prepared materials depending on the Mg content was studied by FT-IR spectroscopy taking Al_2O_3, Ni_6-Mg_7-Al_2O_3, Ni_6-Mg_{15}-Al_2O_3 and Ni_6-Mg_{26}-Al_2O_3 as representative materials. Figure 5 shows the spectra obtained in the 1900-1100 cm^{-1} frequency range (where carbonates signatures appear) after CO_2 adsorption and successive

evacuation at r.t. (Fig. 5, full lines), then 100 °C (Fig. 5, dashed lines) and finally 200 °C (Fig. 5, dotted lines).

For the free carbonate ion, an asymmetric stretch vibration mode ν_3(E) is expected at 1415 cm^{-1}. The lowering of symmetry in the adsorbed state leads to a split in two bands at either sides of 1415 cm^{-1} (ν_{3H} and ν_{3L}, *i.e.* high and low components of the ν_3 vibration) [43], whose splitting ($\Delta\nu_3$) depends on the basic strength (the lower the splitting, the stronger the basic site). Thus, $\Delta\nu_3$ values of ca. 100 cm^{-1} are generally observed for unidentate carbonates (*uc)* formed on strongly basic O^{2-} ions, whereas they are around 300 and > 400 cm^{-1} for chelating bidentate carbonates (*cbc*) and bridging bidentate carbonates (*bbc*) (*i.e.* "organic-like") formed on sites of decreasing basicity or involving the participation of an adjacent cationic site [43, 44]. From this bibliographic knowledge, it is tempting to assign the pairs of bands at 1410/1570 cm^{-1} (★ in Fig. 5) and 1360/1860 cm^{-1} (❖ in Fig. 5) to *uc* and *cbc/bbc* carbonates, respectively (as will be confirmed below). Besides, hydrogen carbonates (*hc*) implying the presence of basic hydroxyl groups can also be present [43-45].

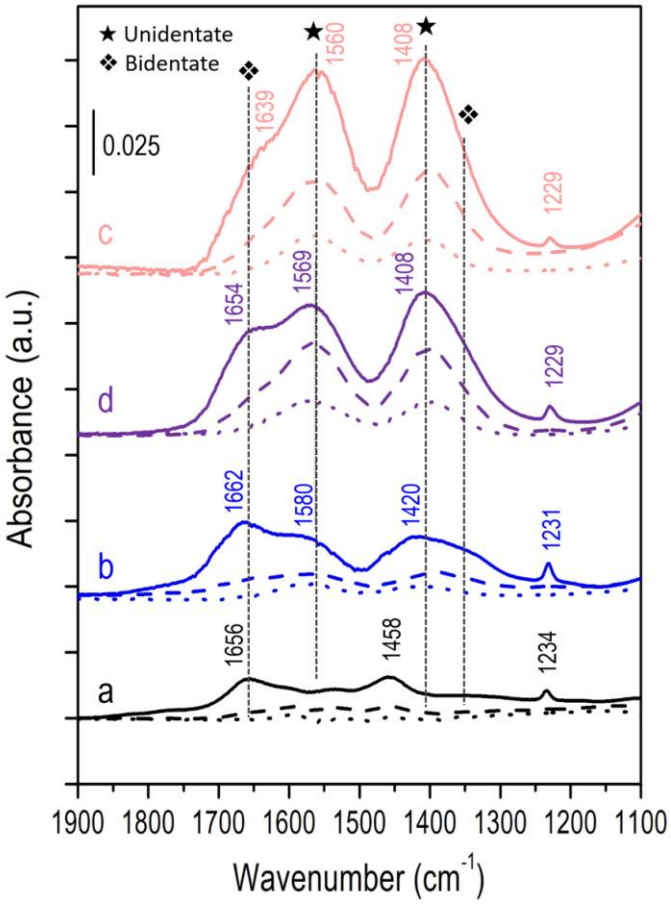

Figure 5. FT-IR spectra obtained in the 1900-1100 cm^{-1} range after exposure of samples (a) Al_2O_3, (b) Ni_6-Mg_7-Al_2O_3, (c) Ni_6-Mg_{15}-Al_2O_3 and (d) Ni_6-Mg_{26}-Al_2O_3 to CO_2 adsorption (7.5 kPa CO_2 equilibrium pressure) then desorption at r.t (full lines), 100 °C (dashed lines) and 200 °C (dotted lines).

After CO_2 adsorption on mesoporous Al_2O_3 and evacuation at r.t., the spectrum shows the occurrence of mainly three weak bands centered at c.a. 1656, 1458 and 1234 cm^{-1} (Fig. 5a, solid line), corresponding to *hc* species (ν_{asym}(O-C-OH)$_{hc}$, ν_{sym}(O-C-OH)$_{hc}$ and δ(C-O-H)$_{hc}$, respectively) and characteristic of the formation of bicarbonates on weakly basic hydroxyls as typically observed on transition aluminas [43-45]. Minor amounts of carbonate species are also detected, in the form of two ν_{3H} bands at 1603 and 1530 cm^{-1}, but they are very weak (visible at high magnification, not shown) and associated to ν_{3L} modes probably overlapped, appearing as a

weak broad absorption between 1365 and 1305 cm^{-1}. This makes difficult any precise assignment of the type of carbonates involved (most likely *cbc* and *uc*). Similarly, residual *bbc* species seem to exist (weak signals at 1820-1770 cm^{-1} and around 1190 cm^{-1}) but they are almost completely desorbed upon outgassing at r.t.. Upon evacuation at higher temperatures, all bands progressively decrease in intensity and they almost disappear at 200 °C (Fig. 5, dotted line) attesting of a weak interaction of CO_2 with the Al_2O_3 sites.

Above bands are still present in the FT-IR spectra of sample Ni_6-Mg_7-Al_2O_3, with a slightly increased intensity for some of them (Fig. 5b). In addition, new overlapping broad bands assignable to (at least) two kinds of carbonate species appear, and are also present with higher intensity for Mg-richer Ni_6-Mg_{15}-Al_2O_3 (Fig. 5c). Their nature was assessed on the basis of their thermal stability (*vide infra*). Firstly, both bands at ca. 1580 and 1410 cm^{-1} somehow persist after evacuation at 200 °C, as is distinctly visualized for Ni_6-Mg_{15}-Al_2O_3 (Fig. 5c, dotted line). In view of their stability and of their split ($\Delta\nu_{3uc} \approx 160$ cm^{-1}), these bands are unambiguously representative of the correlated ν_{3Huc} and ν_{3Luc} modes of unidentate carbonates formed on strong basic sites. Secondly, the shoulder visible at ca. 1350 cm^{-1}, rather corresponds to the ν_{3Lcbc} mode of chelating bidentate carbonates, most probably associated to a ν_{3Hcbc} high-frequency mode overlapping the $\nu_{asym}(O\text{-}C\text{-}OH)_{hc}$ band at 1660 cm^{-1}. This is supported by the disappearance of the signals after evacuation at 200°C for both Ni_6-Mg_7-Al_2O_3 and Ni_6-Mg_{15}-Al_2O_3 (Fig. 5b and 5c, respectively, dotted lines) and by the corresponding high $\Delta\nu_{3cbc}$ split values. Note that very similar bands envelopes were reported for Mg-Al mixed oxides of comparable Mg contents [45].

More strikingly, while the FT-IR bands of unidentate carbonates strongly grow to dominate the IR spectrum when going from Ni_6-Mg_7-Al_2O_3 to Ni_6-Mg_{15}-Al_2O_3 sample (Fig. 5b,c), they no longer increase upon further Mg addition (sample Ni_6-Mg_{26}-Al_2O_3 , Fig. 5d), especially when

comparing the spectra after evacuation at either 100 °C (dashed lines) or 200°C (dotted lines). Moreover, the increase of the Mg content results in *i)* a slight decrease of the integrated absorbance of the δ(C-O-H)$_{hc}$ mode which shifts to a lower frequency (1229 cm^{-1}), in agreement with previous literature on Mg-containing oxides [45, 46], and *ii)* the disappearance of the weak bands due to *bbc*. All these features indicate that the amount of basic O^{2-} sites reaches a maximum after addition of an intermediate amount of magnesium, afterwards their number no longer increases if more Mg is added.

For the sake of completion, more insights on the basic strengths were obtained by comparing the spectra after evacuation at 200 °C. At that temperature, the surface *hc* species were almost completely desorbed, whatever the sample, allowing to satisfactorily curve-fit the spectra using four components with Gaussian profiles. On the one hand, the two central components at c.a. 1580 and 1410 cm^{-1} led to very similar $\Delta\nu_{3uc}$ values of 151, 154 and 163 cm^{-1} (for Ni_6-Mg_7-Al_2O_3, Ni_6-Mg_{15}-Al_2O_3 and Ni_6-Mg_{26}-Al_2O_3, respectively), in the range of those of *uc* species commonly found on strong O^{2-} basic sites. On the other hand, the $\Delta\nu_{3cbc}$ split values between the components of weaker *cbc* species at c.a. 1350 and 1660 cm^{-1} were as expected higher (281, 274 and 320 cm^{-1} for Ni_6-Mg_7-Al_2O_3, Ni_6-Mg_{15}-Al_2O_3 and Ni_6-Mg_{26}-Al_2O_3, respectively), especially for Mg-richer Ni_6-Mg_{26}-Al_2O_3.

3.5 H_2 temperature-programmed studies (H_2-TPR and H_2-TPD)

Reducibility of the calcined samples was identified by temperature programmed reduction (H_2-TPR) carried out from room temperature up to 900°C (Fig. 6A). The absence of peak in the profile of Ni-free mesoporous Al_2O_3 (Fig. 6Aa) agrees with the absence of nickel. For all other samples, a single hydrogen reduction peak is distinctly seen, with a temperature at maximum that varies between 640 and 815 °C depending on the material. The H_2 consumption deduced from

peaks area are always close to the theoretical consumption value of 860 μmol.g^{-1} for 5 wt% Ni, even if a little bit higher for Mg-richest Ni_6-Mg_{26}-Al_2O_3. This confirms the presence of nickel as well as the Ni contents that were also validated by XRF (Table 2). In line with XPS results (showing no Ni enrichment on surfaces), no signal is detected in the temperature range between 300 and 400 °C, revealing the absence of weakly attached NiO nanoparticles on external surfaces [26, 47]. For Ni_6-Al_2O_3 (Fig. 6Ab), the peak is centered around 708 °C, attesting on the contrary of a strong interaction between nickel and its alumina support. Again, this is in favor of the formation of spinel-like $NiAl_2O_4$ species that were previously shown to be reduced above 700°C [47, 48].

When increasing the Mg content to 5 wt% (Fig. 6Ac) then 7wt% (Fig. 6Ad), the maximum of the TPR peak shifts to a slightly lower temperature (around 650 °C) as was already observed and explained by a competitive formation between $NiAl_2O_4$ and $MgAl_2O_4$ clusters, the Mg addition boosting the appearance of $MgAl_2O_4$ species instead of the $NiAl_2O_4$ spinel phase [26]. Nevertheless, as more Mg is added, an additional reduction peak centered around 800 °C starts to appear (Fig. 6Ae, sample Ni_6-Mg_{15}-Al_2O_3) and it becomes predominant when reaching 26 wt% Mg loading (Fig. 6Af, sample Ni_6-Mg_{26}-Al_2O_3). In view of this high Mg content, it was important at this step to ensure that no reduction of MgO (traditionally expected at temperatures above 1000 °C [9, 49]) had taken place. To this end, we submitted a reference Ni-free Mg_{26}-Al_2O_3 material (prepared on purpose) to TPR and obtained an almost – although not totally - flat profile (Fig. 6Ag). This indicated some - but very limited - reduction of the Mg-richest support itself. It may have contributed to the above-mentioned H_2 consumption slightly higher than expected for Ni_6-Mg_{26}-Al_2O_3 (Table 2). Nevertheless, this contribution remains very little. Therefore, it can be concluded that the peak at 800°C is not due to MgO reduction but almost

exclusively to the reduction of nickel at an unusually high temperature. This suggests that nickel, in the Mg-richer material, is no longer present in a spinel phase but is rather embedded within basic mixed oxide NiO-MgO domains (possibly in the form of a NiO-MgO mixed solution) where it is even more strongly stabilized.

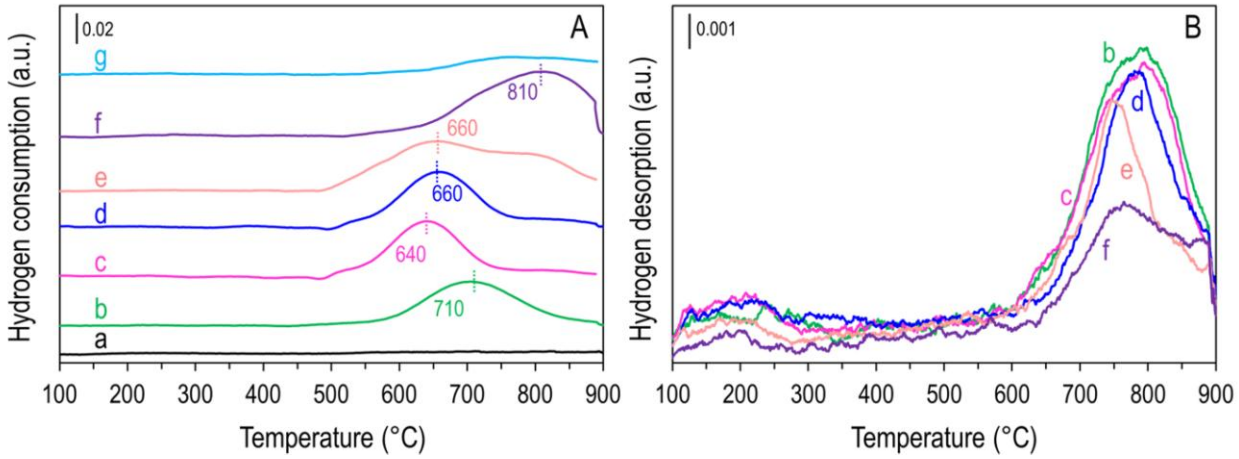

Figure 6: (A) H_2-TPR (calcined samples) and (B) H_2-TPD (reduced samples) profiles of (a) Al_2O_3, (b) Ni_6-Al_2O_3, (c) Ni_6-Mg_5-Al_2O_3 , (d) Ni_6-Mg_7-Al_2O_3, (e) Ni_6-Mg_{15}-Al_2O_3, (f) Ni_6-Mg_{26}-Al_2O_3 and (g) Mg_{26}-Al_2O_3.

After reducing the samples at 650°C, H_2-TPD experiments (also involing H_2 through its dissociatve adsortion on metal sites followed by thermo-programmed desorption) were carried out with the aim to evaluate the number of accessible metal active sites. Whatever the sample, the H_2 desorption profile consisted in a single peak centered around 800 °C (Fig. 6B) indicative of Ni^0 atoms at the surface of the nanoparicles having always high and comparable adsorption strength towards H_2. The area of peaks was used to evaluate the number of such sites in all the catalysts and in turn estimate their apparent mean Ni^0 particles sizes and Ni dispersions. The latter are found to be close and between 16 and 18% in all materials having a Mg content below or equal to 7 wt%, the dispersion then falling as more Mg is added (Table 2).

3.6 Scanning and Transmission Electron Microscopies

The morphology and surface topography of the Ni_6-Mg_x-Al_2O_3 grains in the prepared materials were analyzed by scanning electron microscopy (SEM) taking reduced Ni_6-Al_2O_3, Ni_6-Mg_7-Al_2O_3 and Ni_6-Mg_{26}-Al_2O_3 as representative samples. At low magnification (5k), all materials appear as big blocks (some tenths of μm in size, not shown) but closer observation (Fig. 7) reveals that these blocks consist of aggregations of strongly interconnected smaller porous grains. On Ni_6-Al_2O_3, and to a lesser extent on Ni_6-Mg_7-Al_2O_3, the apertures of the organized channels are clearly seen (insets in Fig. 7a,b, respectively), but not in Ni_6-Mg_{26}-Al_2O_3 whose rough surface shows some lighter aggregates in the mixed detection mode (70% of secondary and 30% of retro-diffused signal, more sensitive to atomic numbers). This might indicate a chemical contrast possibly attributable to external MgO deposits (Fig. 7c). Whatever the sample, the images do not show evidence of any Ni nanoparticle on the surface in spite of the reduced state of the sample, indicating that they are either absent on the surface or too small to be detected by SEM.

To better visualize the porous organization and the size and location of the nickel-based nanoparticles, electron microscopy was also carried in transmission mode at high resolution (HR-TEM) using microtome cuts (50-60nm thickness) to ensure proper observations from the surface to the core of the mesoporous grains constituting the materials. This was done on the same three representative samples as above, which were observed both in their calcined (Fig. 7a'-c') and reduced (Fig. 7a"-c") forms. The image of calcined Ni_6-Al_2O_3 taken at high magnification with beam perpendicular to the orientation of the pores shows distinctly the structured mesoporous channels (Fig. 7a'). When the grains are parallel to the electronic beam, the very regular 2D p6mm hexagonal pore apertures are depicted (inset in Fig. 7a'). Under both orientations, the oxide walls look very regular and there is no evidence of any presence of

individual metal nanoparticles, insisting on the high dispersion already deduced from previous techniques.

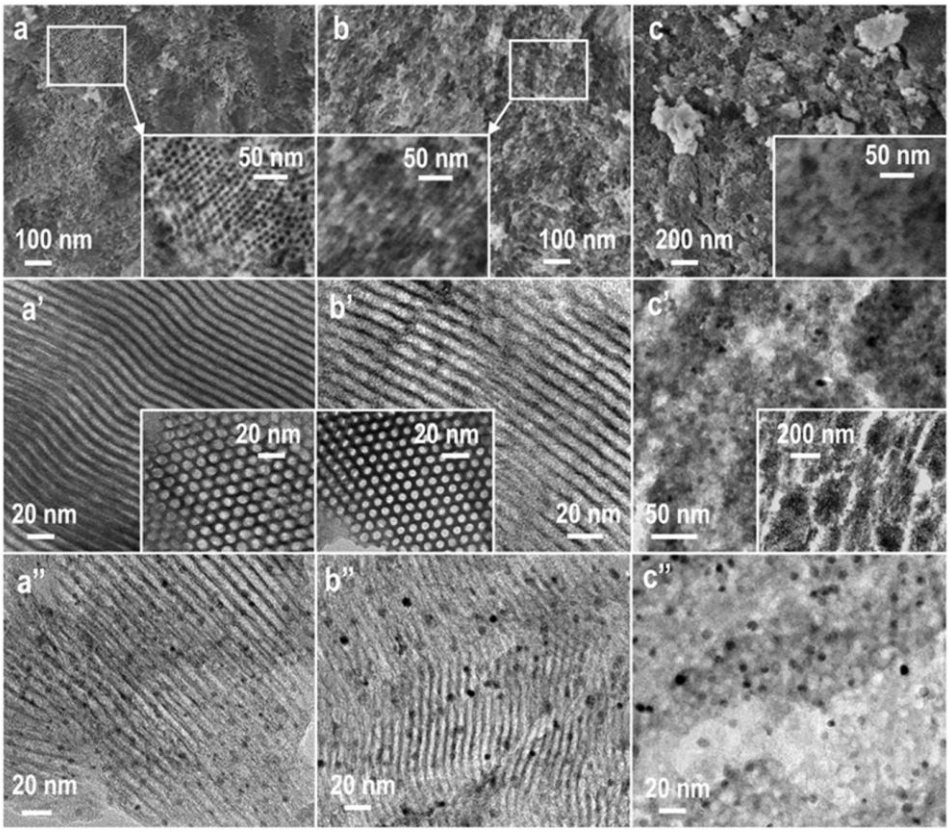

Figure 7: (a-c) SEM and (a'-c',a"-c") HR-TEM images of (a'-c') calcined and (a-c, a"-c") reduced materials: (a-a") Ni_6-Al_2O_3, (b-b") Ni_6-Mg_7-Al_2O_3 and (c-c") Ni_6-Mg_{26}-Al_2O_3.

Increasing the Mg amount to 7 wt% does not alter the well-organized parallel channels and the honeycomb orientation of the alumina pores (Fig. 7b') and the Ni phase is still not detectable. Its presence was however systematically confirmed by local EDX analyses (data not detailed) that also indicated homogeneous nickel content of 5 wt% whatever the analysis area in both calcined Ni_6-Al_2O_3 and Ni_6-Mg_7-Al_2O_3. Conversely, further Mg increment up to 26 wt% (Fig. 7c') clearly contributes to a structural deterioration of the channels and pores and leads to an ill-defined pore morphology. Moreover, few nickel-based nanoparticles with sizes between 4 and 5 nm appear,

attesting of their presence even if they could not be detected by XRD due to the superimposition of the peaks (weak, low Ni amount) with the intense ones of crystalline MgO (Fig. 2Bf). In addition, some components segregation seems to take place in the oxide matrix itself, attested by the appearance of large darker zones (inset in Fig. 7c').

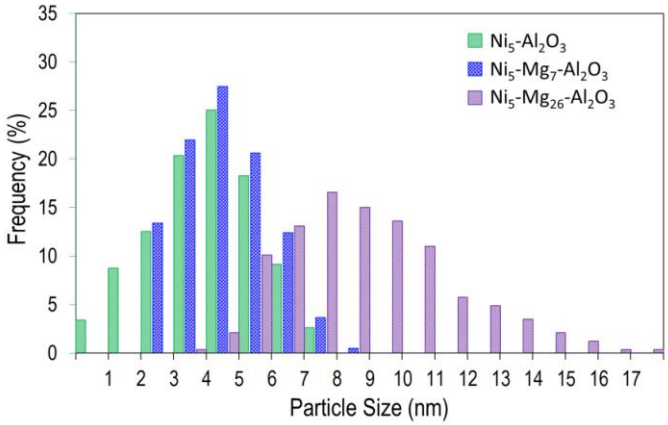

Figure 8: Histograms of Ni^0 particle sizes distributions established from HR-TEM images of the reduced catalysts Ni_6-Al_2O_3 (green), Ni_6-Mg_7-Al_2O_3 (blue) and (c) Ni_6-Mg_{26}-Al_2O_3 (purple)

After reduction at 650°C, TEM images confirm the preservation of the hexagonal mesoporous channel system in both Ni_6-Al_2O_3 and Ni_6-Mg_7-Al_2O_3 (Fig. 7a",b"), although slightly less organized than before reduction. In reduced Ni_6-Mg_{26}-Al_2O_3, the pores are totally disordered and mainly intergranular (Fig. 7c"). Besides, nickel nanoparticles can be seen in all three catalysts, even if hardly visible in Ni_6-Al_2O_3 where they are especially small and seem to stay embedded inside the walls of the mesostructured skeleton (Fig. 7a"). They become more and more distinct as more Mg is added (Fig. 7b",c"). The histograms of particles sizes (Fig. 8) show not only the increase of the Ni^0 nanoparticles but also the enlargement of their sizes ranges when raising the Mg content.

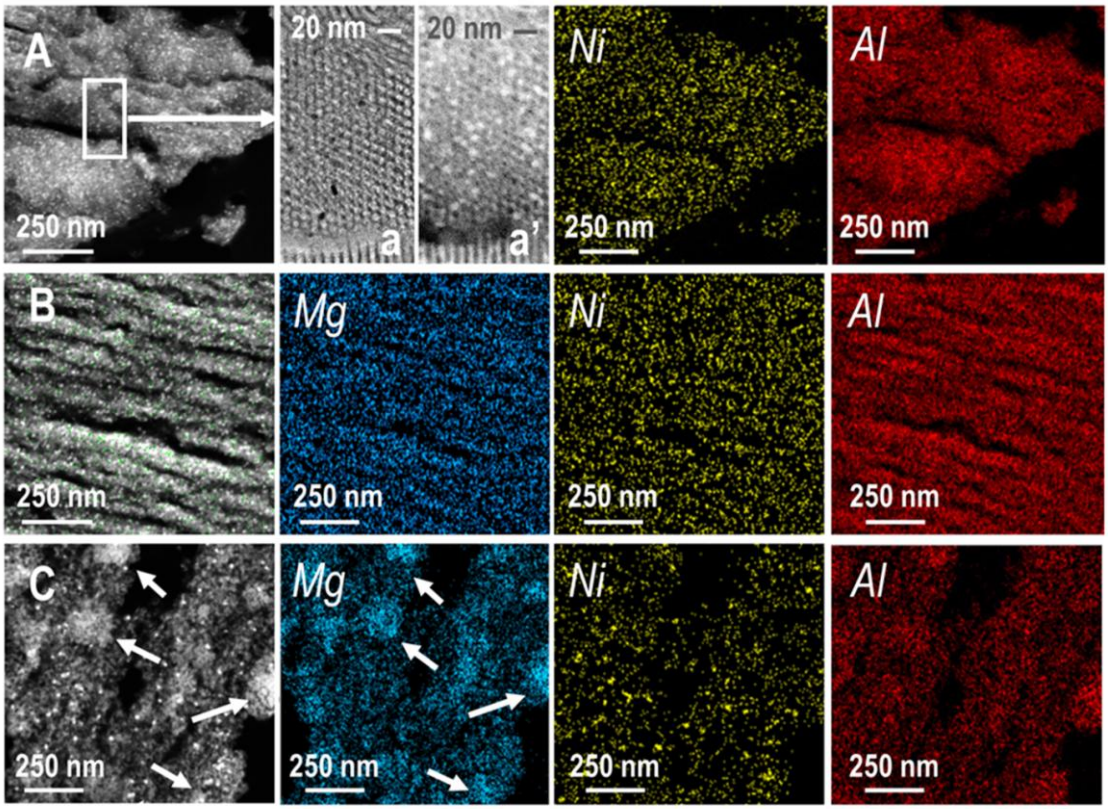

Figure 9: STEM-HAADF images (left) and related STEM-EDX elemental mappings (Mg, Ni and Al) for reduced (A) Ni_6-Al_2O_3, (B) Ni_6-Mg_7-Al_2O_3 and (C) Ni_6-Mg_{26}-Al_2O_3. The Mg mapping is not shown for Mg free Ni_6-Al_2O_3 (top) and replaced by a comparison of zoomed images of a same area observed by (a) HR-TEM and (a') STEM-HAADF.

The presence of very small nanoparticles uneasy to detect in at least two samples even by High-resolution TEM led us to perform additional observations in STEM-HAADF and EDX mapping modes with the hope to better visualize the nickel and Mg distributions. As a reminder, the HAADF technique relies on the atomic number (Z) contrast and can thus be used to discriminate Ni (Z=28) and eventually Mg (Z=12) from the Al (Z=13) component. Considering first the reduced Ni_6-Al_2O_3 (Mg-free) catalyst, the Ni^0 particles are indeed more intelligible on STEM-HAADF images (white dots, Fig. 9A, left) than on HR-TEM ones (Fig. 7a"). This is also illustrated by the comparison of zoomed images of a same zone recorded in either modes (Fig.

9A-a,a'). The nickel nanoparticles appear very well distributed all over the alumina grain, and this is attested as well by EDX mapping that shows a Ni repartition superimposed to Al mapping (Fig. 9A, Ni image). The trends are similar for reduced Ni_6-Mg_7-Al_2O_3 with moreover a homogeneous elemental Mg repartition (Fig. 9B, Mg image). However, this is no longer the case for reduced Ni_6-Mg_{26}-Al_2O_3 that exhibits, on one hand, significantly bigger Ni^0 nanoparticles (Fig. 9C and Table 2) and, on the other hand, bright area in STEM-HAADF and Mg mapping images, corresponding to Mg-rich zones which mean sizes can be estimated as high as few tenths of nm (highlighted by white arrows). Such distinction between the Mg-poor and Mg-rich area in spite of the close atomic number of Mg and Al can be explained by the higher Mg/O atomic ratio of 1 in MgO compared to 2/3 in Al_2O_3 enhancing the local response of the involved elements.

3.7 Catalytic performances

Catalytic tests were first performed on in-situ reduced Ni_6-Al_2O_3 and Ni_6-Mg_7-Al_2O_3 at an hourly gas space velocity of 36 $L.g^{-1}.h^{-1}$ in the range of those traditionally used in the literature (Table 1). In such conditions, CH_4 (Fig. 10Aa,b) and CO_2 (Fig. 10Ba,b) conversions at 650 °C are high on both catalysts (between 60 and 80%), close to thermodynamic equilibrium. This reveals excellent catalytic performances, especially for Ni_6-Mg_7-Al_2O_3 that led to high and very stable CH_4 and CO_2 conversions during 50 h on stream. Some - even if very limited - activity loss was observed on Ni_6-Al_2O_3. This suggests some positive effect of Mg, also attested by a CO_2 conversion very close to that of CH_4 and a H_2/CO values almost equal to 1 on Ni_6-Mg_7-Al_2O_3, indicative of the absence of side reactions (curves b, Fig. 10). By comparison, some methane decomposition took place on Ni_6-Al_2O_3, consuming CH_4 and producing an excess of H_2 (curves

a, Fig. 10). In spite of these tiny differences, the proximity of the reached conversions with those imposed by thermodynamics does not allow a proper comparison of the catalytic performances.

For this reason, a second set of catalytic tests was done at higher GHSV (180 $L.g^{-1}.h^{-1}$) to access lower conversions levels. The multiplication by 5 of the gas space velocity led to a decrease of the conversions by a factor of only 2 or 3 on respectively Ni_6-Mg_7-Al_2O_3 and Ni_6-Al_2O_3 (Fig. 10a,a' and 10c,c'). This absence of proportionality may reveal the occurrence of some diffusional limitations often known to exist in porous catalysts [49]. They however keep limited in our ordered mesoporous materials with low to intermediate Mg contents as deduced from complementary data (not detailed). Therefore, the decreases of conversions by a factor below 5 confirms that part of the active sites was previously not operating and the conversion levels below 40% attained at this higher GHSV allow a more appropriate discrimination between performances. For each catalyst, the CH_4 and CO_2 conversions progressively raised upon heating from r.t. up to 650 °C, in line with the endothermic character of DRM (light off curves, not shown), afterwards the temperature was kept at 650°C for 14h. The results of stability tests show a regular increase of the level of conversions when raising the Mg content from 0 to 5 and then 7 wt% (curves a'-c' in Fig. 10A and 10B for CH_4 and CO_2, respectively), afterwards further Mg addition is no longer beneficial and provokes on the contrary an activity loss, particularly drastic on Ni_6-Mg_{26}-Al_2O_3 (curve e', Fig. 10A and 10B). This loss for the Mg-richest catalyst is also associated to a lowering of the H_2/CO product ratio (below the stoichiometric value of 1) that moreover decreases significantly with time on stream, down to a value as low as 0.5 (Fig. 10Ce'). This decrease suggests a strong occurrence of the Reverse Water Gas Shift (RWGS) side reaction that is known to occur in the same temperature range as DRM and consumes CO_2 and H_2 to produce CO and H_2O [1]. In contrast, the H_2/CO product ratio keeps close to 1 on all other

catalysts, being either slightly below 1 for Ni_6-Al_2O_3 and Ni_6-Mg_{15}-Al_2O_3 (Fig. 10Ca',d'), above one for Ni_6-Mg_5-Al_2O_3 (Fig. 10Cb'), or equal to one for the most active Ni_6-Mg_7-Al_2O_3 catalyst (Fig. 10Cc'). The good catalytic stability observed on all samples (except Ni_6-Mg_{26}-Al_2O_3) suggests a limited coke formation, as deduced from one of our previous work on EISA-one-pot synthesized methane reforming catalysts [36].

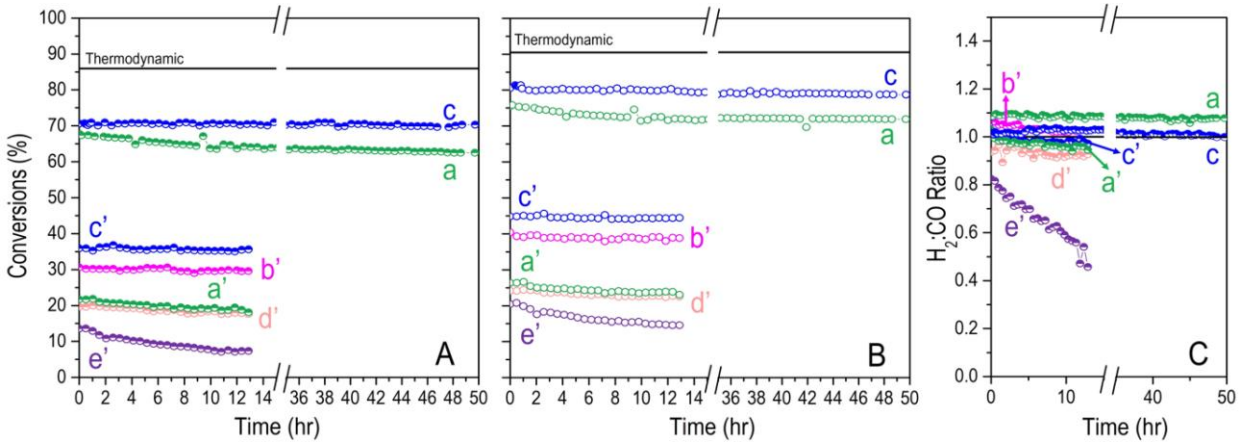

Figure 10: (A) CH_4 conversions, (B) CO_2 conversions and (C) H_2:CO ratios as a function of time during catalytic tests (650°C, 1 atm, CH_4:CO_2 = 1:1) carried out at a GHSV of (a, c) 36 or (a'- e') 180 $L.g^{-1}.h^{-1}$ on the reduced catalysts: (a,a') Ni_6-Al_2O_3, (b') Ni_6-Mg_5-Al_2O_3, (c,c') Ni_6-Mg_7-Al_2O_3, , (d') Ni_6-Mg_{15}-Al_2O_3 and (e') Ni_6-Mg_{26}-Al_2O_3 catalysts. Thermodynamic equilibrium values (black lines).

4. Discussion

4.1 Influence of Mg content on pores ordering in the mesoporous Ni_6-Mg_x-Al_2O_3 materials

In agreement with recent works [33, 34], our results demonstrate that the combination of the Evaporation Induced Self Assembly (EISA) method with the one-pot synthesis allows to produce a hexagonally structured mesoporous Ni-Al_2O_3 material with Ni highly dispersed and stabilized within the alumina matrix. Upon addition of a limited amount of magnesium (till c.a. 7 wt%), the hexagonal network of mesopores is preserved (XRD, N_2 physisorption and electron microscopy

data). A homogeneous Mg repartition is obtained as well (Fig. 8B) and the pores ordering and stability under thermal treatments are even better than in a pure mesoporous Al_2O_3 prepared by the same EISA-one-pot route. This is in line with previous studies reporting that the addition of nitrate in the synthesis medium (present in the nickel and magnesium precursors) ameliorates the structural quality of the formed mesoporous alumina. This might be due to a change of pH that accelerates the hydrolysis of the aluminum precursor and P123 surfactant and favors their coalescence to form micelles while keeping the Al-OH concentration high enough for 2D-hexagonal structure formation [37].

Upon further Mg enrichment (Ni_6-Mg_{15}-Al_2O_3 and Ni_6-Mg_{15}-Al_2O_3 samples), the hexagonally structured porous network is progressively lost, as attested by the alteration of the N_2-soprtion hysteresis loop, the absence of X-ray diffraction peak at low angles and the deterioration of the parallel and hexagonal alumina channels in TEM images. This loss of structural quality can be explained firstly by the fact that the ionic radius of Mg^{2+} (0.72 Å) is larger than that of Al^{3+} (0.54 Å), producing Mg-O bonds longer than the Al-O ones. Thus, the incorporation of a too high amount of Mg^{2+} into the mesoporous alumina framework would result in a meso-structural expansion, hence in a network degradation. Secondly, the merge of the micelle composite in the solution could be perturbed by excessive changes in the chemical composition and pH conditions, leading at high Mg content to disordered materials containing segregated crystalline MgO domains. The MgO crystals are very small in Ni_6-Mg_{15}-Al_2O_3 (very broad and weak XRD peaks, Fig. 3Be) but their mean diameter reaches 5 nm in Ni_6-Mg_{26}-Al_2O_3 (Fig. 3Bf) and they are aggregated, forming Mg rich zones of a few tenths of nm is size (Fig. 9C).

An important impact of the MgO segregation is to produce strongly basic sites able to adsorb CO_2 as unidentate carbonates (*uc)*. The latter are characterized by an intense ν_3 FT-IR doublet

(bands at 1570 and 1410 cm^{-1}) that persists after evacuation at 200 °C. The number of such sites is very low in Ni_6-Mg_7-Al_2O_3, supporting the fact that the Mg^{2+} ions are mainly dispersed within the alumina matrix (as also suggested by transmission electron micrographs). They are more numerous in Ni_6-Mg_{15}-Al_2O_3 in which a segregation of MgO starts to be detected by XRD. However, their amount is maximum at intermediate Mg loading and next decreases upon further Mg addition (Ni_6-Mg_{26}-Al_2O_3). Then, the normalized integrated absorbance of the whole FT-IR bands envelope in the 1800-1100 cm^{-1} range (i.e. amount of basic O^{2-} sites) tends also to decrease (Fig. 11A) due the formation of bulkier MgO crystals with reduced number of basic defective sites at their external surface. (*e.g.* edges and corners). Moreover, this segregation is associated to a loss of structural quality of the material, hindering further the access to adsorption/active sites.

4.2 Impact of Mg on Ni dispersion and Ni-support interaction

After synthesis, the nickel content is close to the expected value of 6 wt% in all Ni_6-Mg_x-Al_2O_3 materials, as deduced from chemical and TPR analyses (Table 2). In spite of its presence, nickel is however detected neither by XRD nor by TEM in calcined Ni_6-Al_2O_3 and Ni_6-Mg_7-Al_2O_3, revealing an extremely high metal dispersion, in contrast with literature that commonly report NiO nanoparticles of few nanometers (between 6 and 12 nm, Table 1) in nickel-magnesium based mesoporous alumina prepared by other methods [21-23, 25]. This suggests an especially strong interaction between nickel and alumina in the EISA-one-pot synthesized Ni_6-Mg_x-Al_2O_3 materials, also deduced from the high reduction temperature (between 650 and 700°C) and from both XRD and XPS data that reveal an intimate mixing between nickel and the alumina matrix in the form of structured spinel nickel-alumina ($NiAl_2O_4$). Such types of nanospecies were recently reported in nickel-alumina synthesized by microwave assisted synthesis [50], atomic layer

deposition [51] or prepared according to a MIL(Al)-53-based route [34, 47]. Upon reduction, nickel is extracted from the $NiAl_2O_4$ nanophases to give homogenously distributed Ni^0 nanoparticles. The latter are detectable by electron microscopy in STEM-HAADF mode but remain very tiny in both Mg free Ni_6-Al_2O_3 and Ni_6-Mg_5-Al_2O_3 catalysts (hardly identified by HR-TEM). This fits our recent proposal that reduced nickel nanoparticles issued from the reduction of $NiAl_2O_4$ nanodomains embedded in the walls are unusually stable against sintering due to a remaining interface made of nickel-aluminate-like (or related phase) acting as a "glue" between Ni^0 and the alumina walls after reduction able to strongly reinforce the metal-support interaction as also recently observed in mesoporous Ni-alumina catalysts prepared from MIL-53(Al) [34, 47].

The mean size of the Ni^0 particles tends to grow as more Mg is added as revealed by all techniques used for particles size estimation (Table 2 and Fig. 11B). According to H_2-TPD data, the Ni dispersion varies from about 20% (5.2 nm Ni^0 mean size) for Ni_6-Al_2O_3 to less than 7% (14 nm Ni^0 mean size) for Ni_6-Mg_{26}-Al_2O_3. These mean size values are however systematically higher than when estimated by TEM or XRD, especially at high Mg content. Hence, not all nickel sites (expected to be the H_2 adsorption sites), would be accessible. For the Mg-poor samples, the discrepancy remains small and it is consistent with the above hypothesis that some nickel atoms are trapped at the interface between the Ni^0 nanoparticles and the alumina walls. The reasons why it is much higher for Mg-rich Ni_6-Mg_{26}-Al_2O_3 might be twofold. On one hand, it could be related to the significant loss of pores ordering, reducing the access to Ni^0 nanoparticles. On the other hand, part of nickel could be occluded in seggregated NiO-MgO nanodomains, in line with the unusually high reduction temperature (above 800 °C for Ni_6-Mg_{26}-Al_2O_3) that attest of the strong interaction of nickel with its close vicinity (here the basic MgO

phase) [22]. The increase in basicity could also play a role by keeping the Ni^0 nanoparticles partially oxidized (local charge transfer). Thus, the loss of metallic character would make the particle less active for H_2 adsorptive dissociation [52]. Finally, it is worth recalling that mainly NiO (instead of $NiAl_2O_4$) was detected in calcined Ni_6-Mg_{26}-Al_2O_3 (by both XRD and TEM) and the supported nickel-based nanoparticles were quite unstable and sensitive to sintering. Thus, their mean diameter almost doubled after reduction (Table 2) in spite of the smaller size expected for a Ni^0 compared to a NiO particle (containing respectively only Ni or both Ni and O).

4.3 Reasons of an optimum Mg content for best catalytic performances in DRM

The present study finally confirms the volcano behavior suggested by literature during DRM reaction. It consists in a regular gain of CH_4 and CO_2 conversions when introducing Mg into mesoporous Nickel alumina catalysts up to a certain level, afterwards an activity loss takes place if too much Mg is added (Fig. 1 for bibliography and Fig. 11C for our work). Due to distinct Ni dispersions and therefore distinct number of active sites in the catalysts, a more appropriate comparison of sites activity relies on Turn-Over-Frequencies that were estimated from conversions and nickel dispersion values, as detailed in section 2.3, for the whole Ni_6-Mg_x-Al_2O_3 series of catalysts. Interestingly, the plot of TOFs as a function of the Mg content still shows a volcano trend, with values varying between 2.50 s^{-1} and 5.81 s^{-1} and a maximum positioned at an intermediate Mg amount, between 5 and 10 wt% of Mg (Fig. 11D). Thus, conversion levels not only depend on nickel dispersion and active sites accessibility but also on the intrinsic sites activity that is maximum at intermediate Mg content.

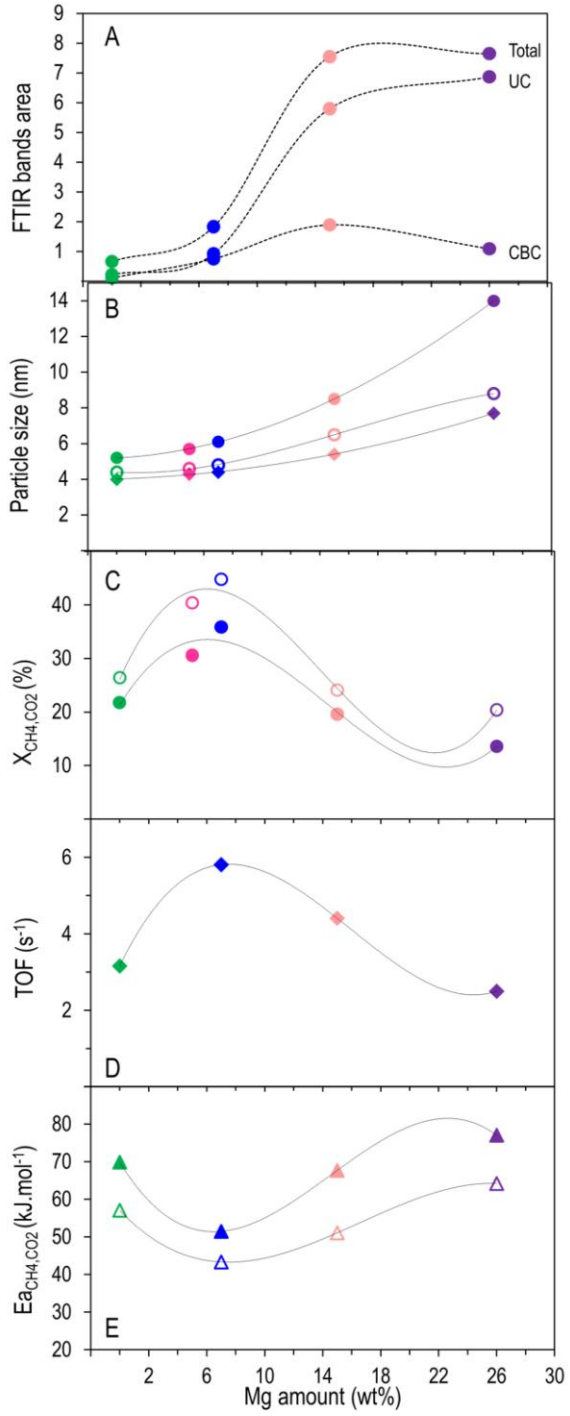

***Figure 11**: Evolution as a function of the Mg content of; (A) FTIR bands area; (B) Ni^0 dispersion estimated from (Δ) XRD, (o) HRTEM, and (•) H_2-TPD measurements; (C, D, E) catalytic performances expressed as Turn-Over Frequency (TOF), CH_4 conversion (X_{CH4}), CO_2 conversion (X_{CO2}) and apparent activation energy for CH_4 (Ea_{CH4}) and CO_2 (Ea_{CO2}) consumptions.*

At this point, it can be recalled that methane dissociation in DRM occurs on Ni sites (forming CHx intermediates) while carbon dioxide is adsorbed and activated on the surface sites of the oxide support. The expected positive role of basic sites is to increase the rate of activation of CO_2 [53] with intermediate formation of carbonates. A previous *in-situ* DRIFT study of rare earth promoted Ni-Mg-Al catalysts concluded to the involvement of two types of carbonates, i.e. monodentate and bidentate carbonates that react effectively with deposited carbon during DRM and enhance the catalytic stability [54]. In the same study, it was also proposed that bidentate carbonates are more favorable for CHx conversion because of being less stable (i.e. more reactive). Such carbonates are similarly present in our mesoporous Ni_6-Mg_x-Al_2O_3 catalysts (identified as *uc* and *cbc*, respectively, see section 3.4), and not only their global content but more specifically the amount of *cbc* are the highest at intermediate Mg loading (Fig. 11A). In addition, they coexist with weakly stable hydroxy-carbonates (*hc*).

These basicity features fit well the evolution of the apparent activation energies for CO_2 conversion ($EaCO_2$) on the Ni_6-Mg_x-Al_2O_3 series of catalysts (Figure 11E). Firstly, their values (between 40 and 75 KJ.mol^{-1}) are within the range of Ea_aCO_2 values reported for nickel-based catalysts that significantly vary depending on the support properties, nature of promoters or catalytic tests conditions applied (Table S1). In the present work, the values keep at the bottom range, attesting of the efficiency of the catalysts towards CO_2 activation (no internal diffusion as demonstrated by Weisz-Prater criterion, SI). More importantly, the variation of Ea_aCO_2 as a function of the Mg wt% shows a reverse volcano curve (Fig. 11E) and the lowest Ea_aCO_2 value (easier CO_2 activation) is obtained at an intermediate Mg loading (5-10 wt %), in a range where accessible medium basic sites are also the most numerous.

This positive basicity effect could contribute as well to the decrease of the $EaCH_4$ value (down to 51 kJ.mol^{-1} for Ni_6-Mg_7-Al_2O_3) by facilitating the reaction of the formed CH* intermediates with activated CO_2 adsorbates, limiting in turn coke formation. It should be kept in mind, however, that CH_4 activation occurs on Ni^0 metal sites whose electronic behavior and therefore intrinsic activity could be also affected. If present, such effect would be nevertheless expected to rather decrease the metallic character of the nanoparticles than increasing it, having most likely a negative effect on methane decomposition. It is also worth noting that the $EaCH_4$ values are above the $EaCO_2$ ones, showing that the activation of CH_4 is the rate limiting step on those catalysts. Combined to the basicity effect discussed above, the increase of both $EaCO_2$ and $EaCH_4$ when adding too much Mg might be also related to the high RWGS occurrence (Ni_6-Mg_{26}-Al_2O_3 catalyst), attested by the drastic fall of the H_2/CO product ratio (Fig. 10Ce'), retarding and hindering the activity of the main reaction [55]. In addition, the loss of structural ordering and porosity in Mg rich samples plays a detrimental role, by hindering the accessibility to the CO_2 and Ni^0 activation sites [23] which are moreover less numerous (low Ni dispersion and high Mg segregation).

5. Conclusion

In this work, we demonstrate the importance of controlling the amount of Mg added in porous nickel-alumina catalysts to optimize their catalytic performances in Dry Reforming of Methane. With respect to the prepared organized mesoporous materials, four main physico-chemical properties are found to be crucial: i) preservation of a high surface area favorable to active sites dispersion, ii) maintenance of a hexagonal mesopores ordering that ensures easy access to the sites (both basic and metal ones), iii) generation of basic sites to facilitate the adsorptive activation of CO_2 expected to react with the intermediate carbonaceous species (or deposits)

formed during DRM and iv) preservation of the nickel dispersion after reduction and during reaction. To fit all these constraints, we demonstrate that Mg addition is indeed positive by providing basic sites in the material, but the Mg content should be controlled and kept at an intermediate level (between 5 and 10 wt% in the present Ni_6-Mg_x-Al_2O_3 series of materials) in order to avoid MgO segregation that occurs at high Mg contents and leads to the aggregation of big MgO crystals. This provokes a loss of structural ordering, a decrease of the specific surface and a loss of accessible sites (both basic and metal ones). Moreover, it generates the presence of mainly strong basic sites instead of intermediates ones (forming respectively unidendate carbonates *(uc)* and bidentate carbonates *(cbc)* upon CO_2 adsorption) while the latter are more appropriate for the reaction because being slightly less stable and hence more reactive towards intermediate carbonaceous species (deposits) during DRM. In addition, using the EISA-one-pot synthesis method, and as long as the Mg content does not exceed the intermediate content discussed above, nickel in the calcined samples is present in the form of spinel nickel-aluminate nanospecies embedded within the alumina walls, leading after reduction to small and unusually stable Ni^0 nanoparticles that are assumed to interact with the support by a remaining interface. These features are lost in the Mg-rich calcined materials in which NiO (less stable) as well as mixed NiO-MgO domains (in which Ni is no longer accessible) are found to exist. In agreement with their physicochemical properties (preserved hexagonal mesopores, high Ni dispersion, basic sites of intermediate strength, sites accessibility), the catalysts with intermediate Mg contents show the highest conversions, highest TOFs values and lowest activation energies. They are also highly stable and selective to the targeted DRM reaction.

Acknowledgements

This research was carried out during the SOL-CARE (Energy-065) project developed in the frame of the EU-FP7 ERANETMED initiative (JC-Energy-2014 call) and financially supported by the ANR (France) and the CNRS-L and UOB Research Council (Lebanon). The authors are grateful to Antoine Miche (Sorbonne University) and Roberto Nasi (Politecnico di Torino) for their respective contributions on XPS and FT-IT measurements.

References:

1. J. Lavoie, F.G. Labiano, Review on dry reforming of methane , a potentially more environmentally-friendly approach to the increasing natural gas exploitation, Front. Chem. 2 (2014) 1–17. doi:10.3389/fchem.2014.00081.
2. D. Pakhare, J. Spivey, A review of dry (CO2) reforming of methane over noble metal catalysts, Chem. Soc. Rev. 43 (2014) 7813–7837. doi:10.1039/C3CS60395D.
3. Y. Gao, J. Jiang, Y. Meng, F. Yan, A. Aihemaiti, A review of recent developments in hydrogen production via biogas dry reforming, Energy Convers. Manag. 171 (2018) 133–155. doi:10.1016/j.enconman.2018.05.083.
4. M.H. Amin, K. Mantri, J. Newnham, J. Tardio, S.K. Bhargava, Highly stable ytterbium promoted Ni/γ-Al2O3 catalysts for carbon dioxide reforming of methane, Appl. Catal. B Environ. 119–120 (2012) 217–226. doi:10.1016/j.apcatb.2012.02.039.
5. M. Barroso-quiroga, A.E. Castro-luna, Catalytic activity and effect of modifiers on Ni-based catalysts for the dry reforming of methane, Int. J. Hydrogen Energy. 35 (2010) 6052–6056. doi:10.1016/j.ijhydene.2009.12.073.
6. J.W. Han, J.S. Park, M.S. Choi, H. Lee, Uncoupling the size and support effects of Ni

catalysts for dry reforming of methane, Appl. Catal. B Environ. 203 (2017) 625–632. doi:10.1016/j.apcatb.2016.10.069.

7. X. Li, Y. Huang, Q. Zhang, C. Luan, V.A. Vinokurov, W. Huang, Highly stable and anti-coking Ni/MoCeZr/MgAl2O4-MgO complex support catalysts for CO2 reforming of CH4: Effect of the calcination temperature, Energy Convers. Manag. 179 (2019) 166–177. doi:10.1016/j.enconman.2018.10.067.
8. J. Zhang, M. Ren, X. Li, Q. Hao, H. Chen, X. Ma, Ni-based catalysts prepared for CO2 reforming and decomposition of methane, Energy Convers. Manag. 205 (2020) 112419. doi:10.1016/j.enconman.2019.112419.
9. Y.H. Hu, Solid-solution catalysts for CO2 reforming of methane, Catal. Today. 148 (2009) 206–211. doi:10.1016/j.cattod.2009.07.076.
10. L. Karam, N. El Hassan, Advantages of mesoporous silica based catalysts in methane reforming by CO 2 from kinetic perspective, J. Environ. Chem. Eng. 6 (2018) 4289–4297. doi:10.1016/j.jece.2018.06.031.
11. S. Damyanova, B. Pawelec, K. Arishtirova, J.L.G. Fierro, C. Sener, T. Dogu, MCM-41 supported PdNi catalysts for dry reforming of methane, Appl. Catal. B Environ. 92 (2009) 250–261. doi:10.1016/j.apcatb.2009.07.032.
12. X. Lv, J. Chen, Y. Tan, Y. Zhang, A highly dispersed nickel supported catalyst for dry reforming of methane, Catal. Commun. 20 (2012) 6–11. doi:10.1016/j.catcom.2012.01.002.
13. L. Karam, S. Casale, H. El Zakhem, N. El Hassan, Tuning the properties of nickel nanoparticles inside SBA-15 mesopores for enhanced stability in methane reforming, J. CO2 Util. 17 (2017) 119–124. doi:10.1016/j.jcou.2016.12.002.

14. M. Zhang, J. Zhang, X. Zhang, Z. Zhou, F. Song, Q. Zhang, Y. Tan, Y. Han, How the reflux treatment stabilizes the metastable structure of ZrO2 and improves the performance of Ni/ZrO2 catalyst for dry reforming of methane?, Energy Convers. Manag. 216 (2020). doi:10.1016/j.enconman.2020.112950.
15. M.N. Kaydouh, N. El Hassan, A. Davidson, S. Casale, H. El Zakhem, P. Massiani, Highly active and stable Ni/SBA-15 catalysts prepared by a “two solvents” method for dry reforming of methane, Microporous Mesoporous Mater. 220 (2016) 99–109. doi:10.1016/j.micromeso.2015.08.034.
16. Q. Ma, Y. Han, Q. Wei, S. Makpal, X. Gao, J. Zhang, T.S. Zhao, Stabilizing Ni on bimodal mesoporous-macroporous alumina with enhanced coke tolerance in dry reforming of methane to syngas, J. CO2 Util. 35 (2020) 288–297. doi:10.1016/j.jcou.2019.10.010.
17. M. Lu, X. Zhang, J. Deng, S. Kuboon, K. Faungnawakij, S. Xiao, D. Zhang, Coking-resistant dry reforming of methane over BN-nanoceria interface-confined Ni catalysts, Catal. Sci. Technol. 10 (2020) 4237–4244. doi:10.1039/d0cy00537a.
18. P. Chen, Z.-Y. Hou, X.-M. Zheng, Production of Synthesis Gas via Methane Reforming with CO2 on Ni/SiO2 Catalysts Promoted by Alkali and Alkaline Earth Metals, Chinese J. Chem. 23 (2005) 847–851. doi.org/10.1002/cjoc.200590847.
19. R. Yang, C. Xing, C. Lv, L. Shi, N. Tsubaki, Promotional effect of La2O3 and CeO2 on Ni/γ-Al2O3 catalysts for CO2 reforming of CH4, Appl. Catal. A Gen. 385 (2010) 92–100. doi:10.1016/j.apcata.2010.06.050.
20. H. Arbag, Effect of impregnation sequence of Mg on performance of mesoporous alumina supported Ni catalyst in dry reforming of methane, Int. J. Hydrogen Energy. 43

(2018) 6561–6574. doi:10.1016/j.ijhydene.2018.02.063.

21. H.S. Roh, K.W. Jun, Carbon dioxide reforming of methane over Ni catalysts supported on Al 2O3 modified with La2O3, MgO, and CaO, Catal. Surv. from Asia. 12 (2008) 239–252. doi:10.1007/s10563-008-9058-0.
22. J.-E. Min, Y.-J. Lee, H.-G. Park, C. Zhang, K.-W. Jun, Carbon dioxide reforming of methane on Ni–MgO–Al2O3 catalysts prepared by sol–gel method: Effects of Mg/Al ratios, J. Ind. Eng. Chem. 26 (2015) 375–383. doi:10.1016/j.jiec.2014.12.012.
23. L. Zhang, Q. Zhang, Y. Liu, Y. Zhang, Dry reforming of methane over Ni/MgO-Al2O3 catalysts prepared by two-step hydrothermal method, Appl. Surf. Sci. 389 (2016) 25–33. doi:10.1016/j.apsusc.2016.07.063.
24. Y. Zhan, J. Han, Z. Bao, B. Cao, Y. Li, J. Street, F. Yu, Biogas reforming of carbon dioxide to syngas production over Ni-Mg-Al catalysts, Mol. Catal. 436 (2017) 248–258. doi:10.1016/j.mcat.2017.04.032.
25. Z. Hou, T. Yashima, Meso-porous Ni/Mg/Al catalysts for methane reforming with CO2, Appl. Catal. A Gen. 261 (2004) 205–209. doi:10.1016/j.apcata.2003.11.002.
26. N.D. Charisiou, A. Baklavaridis, V.G. Papadakis, M.A. Goula, Synthesis gas production via the biogas reforming reaction over Ni/MgO-Al2O3 and Ni/CaO-Al2O3 catalysts, Waste Biomass Valorization. 7 (2016) 725–736. doi.org/10.1007/s12649-016-9627-9.
27. B. Rego de Vasconcelos, D. Pham Minh, N. Lyczko, T.S. Phan, P. Sharrock, A. Nzihou, Upgrading greenhouse gases (methane and carbon dioxide) into syngas using nickel-based catalysts, Fuel. 226 (2018) 195–203. doi:10.1016/j.fuel.2018.04.017.
28. W. Cai, J. Yu, C. Anand, A. Vinu, M. Jaroniec, Facile synthesis of ordered mesoporous alumina and alumina-supported metal oxides with tailored adsorption and framework

properties, Chem. Mater. 23 (2011) 1147–1157. doi:10.1021/cm102512v.

29. L. Xu, H. Song, L. Chou, Ordered mesoporous MgO-Al2O3 composite oxides supported Ni based catalysts for CO2 reforming of CH4 : Effects of basic modifier and mesopore structure, Int. J. Hydrogen Energy. 38 (2013) 7307–7325. doi:10.1016/j.ijhydene.2013.04.034.
30. X. Fang, C. Peng, H. Peng, W. Liu, X. Xu, X. Wang, C. Li, W. Zhou, Methane Dry Reforming over Coke-Resistant Mesoporous Ni-Al2O3 Catalysts Prepared by Evaporation-Induced Self-Assembly Method, ChemCatChem. 7 (2015) 3753–3762. doi:10.1002/cctc.201500538.
31. N. Wang, K. Shen, L. Huang, X. Yu, W. Qian, W. Chu, Facile route for synthesizing ordered mesoporous Ni-Ce-Al oxide materials and their catalytic performance for methane dry reforming to hydrogen and syngas, ACS Catal. 3 (2013) 1638–1651. doi:10.1021/cs4003113.
32. X. Huang, C. Ji, C. Wang, F. Xiao, N. Zhao, N. Sun, W. Wei, Y. Sun, Ordered mesoporous CoO-NiO-Al2O3 bimetallic catalysts with dual confinement effects for CO2 reforming of CH4, Catal. Today. 281 (2017) 241–249. doi:10.1016/j.cattod.2016.02.064.
33. K. Jabbour, P. Massiani, A. Davidson, S. Casale, N. El Hassan, Ordered mesoporous “one-pot” synthesized Ni-Mg (Ca)-Al 2 O 3 as effective and remarkably stable catalysts for combined steam and dry reforming of methane (CSDRM)., Appl. Catal. B Environ. 201 (2017) 527–542. doi.org/10.1016/j.apcatb.2016.08.009.
34. L. Karam, J. Reboul, N. El Hassan, J. Nelayah, P. Massiani, Nanostructured nickel aluminate as a key intermediate for the production of highly dispersed and stable nickel nanoparticles supported within mesoporous alumina for dry reforming of methane,

Molecules. 24 (2019) 4107-4120. doi:10.3390/molecules24224107.

35. S.M. Morris, P.F. Fulvio, M. Jaroniec, Ordered mesoporous alumina-supported metal oxides, J. Am. Chem. Soc. 130 (2008) 15210–15216. doi:10.1021/ja806429q.
36. M. Thommes, K. Kaneko, A. V Neimark, J.P. Olivier, F. Rodriguez-reinoso, J. Rouquerol, K.S.W. Sing, Physisorption of gases , with special reference to the evaluation of surface area and pore size distribution (IUPAC Technical Report), Pure Appl. Chem. 87 (2015) 1051–1069. doi:10.1515/pac-2014-1117.
37. D. Pan, Z. Dong, M. He, W. Chen, S. Chen, F. Yu, B. Fan, X. Cui, R. Li, Structural and surface properties of highly ordered mesoporous magnesium-aluminium composite oxides derived from facile synthesis, Mater. Chem. Phys. 186 (2017) 574–583. doi:10.1016/j.matchemphys.2016.11.038.
38. V. Meynen, P. Cool, E.F. Vansant, Verified syntheses of mesoporous materials, Microporous Mesoporous Mater. 125 (2009) 170–223. doi:10.1016/j.micromeso.2009.03.046.
39. A. Grosman, C. Ortega, Capillary condensation in porous materials. Hysteresis and interaction mechanism without pore blocking/percolation process, Langmuir. 24 (2008) 3977–3986. doi:10.1021/la703978v.
40. N. Wang, X. Yu, K. Shen, W. Chu, W. Qian, Synthesis, characterization and catalytic performance of MgO-coated Ni/SBA-15 catalysts for methane dry reforming to syngas and hydrogen, Int. J. Hydrogen Energy. 38 (2013) 9718–9731. doi:10.1016/j.ijhydene.2013.05.097.
41. L. Xu, H. Zhao, H. Song, L. Chou, Ordered mesoporous alumina supported nickel based catalysts for carbon dioxide reforming of methane, Int. J. Hydrogen Energy. 37 (2012)

7497–7511. doi:10.1016/j.ijhydene.2012.01.105.

42. N.D. Charisiou, L. Tzounis, V. Sebastian, S.J. Hinder, M.A. Baker, K. Polychronopoulou, Investigating the correlation between deactivation and the carbon deposited on the surface of Ni/Al2O3 and Ni/La2O3 -Al 2O3 catalysts during the biogas reforming reaction, Appl. Surf. Sci. 474 (2019) 42–56. doi:10.1016/j.apsusc.2018.05.177.
43. J.C. Lavalley, Infrared spectrometric studies of the surface basicity of metal oxides and zeolites using adsorbed probe molecules, Catal. Today. 27 (1996) 377–401. doi:10.1016/0920-5861(95)00161-1.
44. G. Busca, V. Lorenzelli, Infrared spectroscopic identification of species arising from reactive adsorption of carbon oxides on metal oxide surfaces, Mater. Chem. 7 (1982) 89–126. doi:10.1016/0390-6035(82)90059-1.
45. H.A. Prescott, Z.J. Li, E. Kemnitz, A. Trunschke, J. Deutsch, H. Lieske, A. Auroux, Application of calcined Mg-Al hydrotalcites for Michael additions: An investigation of catalytic activity and acid-base properties, J. Catal. 234 (2005) 119–130. doi:10.1016/j.jcat.2005.06.004.
46. J.A. Lercher, C. Colombier, H. Noller, Acid-Base Properties of Alumina-Magnesia Mixed Oxides, J. Chem. Soc. Faraday Trans. 80 (1984) 949–959. doi.org/10.1039/F19848000949
47. L. Karam, J. Reboul, S. Casale, N. El Hassan, P. Massiani, Porous nickel-alumina derived from metal-organic framework (MIL-53): a new approach to achieve active and stable catalysts in methane dry reforming, ChemCatChem. 12 (2019) 373-385. https://doi.org/10.1002/cctc.201901278
48. M. Gil-Calvo, C. Jiménez-González, B. de Rivas, J.I. Gutiérrez-Ortiz, R. López-Fonseca,

Effect of Ni/Al molar ratio on the performance of substoichiometric NiAl2O4 spinel-based catalysts for partial oxidation of methane, Appl. Catal. B Environ. 209 (2017) 128–138. doi:10.1016/j.apcatb.2017.02.063.

49. R.K. Singha, A. Shukla, A. Sandupatla, G. Deo, R. Bal, Synthesis and catalytic activity of a Pd doped Ni-MgO catalyst for dry reforming of methane, J. Mater. Chem. A. 5 (2017) 15688–15699. doi:10.1039/c7ta04452f.
50. A.A.S. Gonçalves, M.J.F. Costa, L. Zhang, F. Ciesielczyk, M. Jaroniec, One-Pot Synthesis of MeAl2O4 (Me = Ni, Co, or Cu) Supported on γ-Al2O3 with Ultralarge Mesopores: Enhancing Interfacial Defects in γ-Al2O3 to Facilitate the Formation of Spinel Structures at Lower Temperatures, Chem. Mater. 30 (2018) 436–446. doi:10.1021/acs.chemmater.7b04353.
51. P. Littlewood, S. Liu, E. Weitz, T.J. Marks, P.C. Stair, Ni-Alumina Dry Reforming Catalysts: Atomic Layer Deposition and the Issue of Ni Aluminate, Catal. Today. 343 (2020) 18-25. doi:10.1016/j.cattod.2019.03.040.
52. H. Özdemir, M.A. Faruk Öksüzömer, M. Ali Gürkaynak, Preparation and characterization of Ni based catalysts for the catalytic partial oxidation of methane: Effect of support basicity on H2/CO ratio and carbon deposition, Int. J. Hydrogen Energy. 35 (2010) 12147–12160. doi:10.1016/j.ijhydene.2010.08.091.
53. T. Harada, F. Simeon, E.Z. Hamad, T.A. Hatton, Alkali metal nitrate-promoted high-capacity MgO adsorbents for regenerable CO2 capture at moderate temperatures, Chem. Mater. 27 (2015) 1943–1949. doi:10.1021/cm503295g.
54. Y. Cao, H. Li, J. Zhang, L. Shi, D. Zhang, Promotional effects of rare earth elements (Sc, Y, Ce, and Pr) on NiMgAl catalysts for dry reforming of methane, RSC Adv. 6 (2016)

112215–112225. doi:10.1039/c6ra19139h.

55. Ş. Özkara-Aydinoğlu, A. Erhan Aksoylu, A comparative study on the kinetics of carbon dioxide reforming of methane over Pt-Ni/Al2O3catalyst: Effect of Pt/Ni Ratio, Chem. Eng. J. 215–216 (2013) 542–549. doi:10.1016/j.cej.2012.11.034.